2D dry granular free-surface transient flow over complex topography with obstacles. Part II: numerical predictions of fluid structures and benchmarking

C. Juez, D. Caviedes-Voullième, J. Murillo and P. García-Navarro[a,*]

[a] *LIFTEC, CSIC-Universidad de Zaragoza, Spain*

Abstract

Dense granular flows are present in geophysics and in several industrial processes, which has lead to an increasing interest for the knowledge and understanding of the physics which govern their propagation. For this reason, a wide range of laboratory experiments on gravity-driven flows have been carried out during the last two decades. The present work is focused on geomorphological processes and, following previous work, a series of laboratory studies which constitute a further step in mimicking natural phenomena are described and simulated. Three situations are considered with some common properties: a two-dimensional configuration, variable slope of the topography and the presence of obstacles. The setup and measurement technique employed during the development of these experiments are deeply explained in the companion work. The first experiment is based on a single obstacle, the second one is performed against multiple obstacles and the third one study the influence of a dike on which overtopping occurs. Due to the impact of the flow against the obstacles, fast moving shocks appear, and a variety of secondary waves emerge. In order to delve into the physics of this type of phenomena, a shock-capturing numerical scheme is used to simulate the cases. The suitability of the mathematical models employed in this work has been previously validated. Comparisons between computed and experimental data are presented for the three cases. The computed results show that the numerical tool is able to predict faithfully the overall behavior of this type of complex dense granular flow.

*carmelo@unizar.es

Manuscript accepted in *Computers and Geosciences* *April 3, 2014*

Keywords: Granular flow, Landslides, Numerical modeling, Obstacles

1. Introduction

The study of landslides and their movement constitutes an important environmental issue as they play a key role in landscape evolution. Currently, the triggering mechanisms, mechanical properties and assessment of likelihood and consequences as well as the development of measures to limit their impact, is an active topic in the field of the geophysical flows research.

These geophysical flows are essentially a mass of solid grains within a less dense intergranular fluid such as water or gas. This type of mixture is classified in three different regimes as was pointed out by Pouliquen and Forterre (2008): a dense quasi-static regime in which grain deformations can be neglected and the frictional forces govern the movement, a gaseous regime in which the grains present a strong agitation and the collision forces are predominant and an intermediate liquid regime in which the material is dense but flows like a fluid and collision and frictional forces are in the same order of importance. If it is assumed that the concentration of grains within the flow is high enough, then the frictional forces govern the momentum transport. Therefore, dry granular flows are the most suitable candidates for studying this type of geophysical phenomena.

Due to the fact that avalanches are initiated on steep slopes, pioneer experimental studies concerning granular flows were focused on the grain movement over constant inclined planes with slopes larger than the material repose angle (Wieland et al., 1999; Pouliquen, 1999; Pouliquen and Forterre, 2002; Mangeney et al., 2010). This type of movement is governed by the gravity component along the slope direction. Experiments developed in Pouliquen (1999); Mangeney et al. (2010) were performed over a genuine 1D configuration whilst Wieland et al. (1999); Pouliquen and Forterre (2002) were devoted to 2D events. All of them brought the opportunity of studying unstable granular masses, focusing on the maximum spreading or the avalanche front and tail speeds.

Additionally to these prior laboratory works, in Lajeunesse et al. (2004); Boutreux and deGennes (1997) other type of configuration was experimentally addressed: the sudden release of a surface over a quasi-horizontal surface. In such case, the weight of the sand grains was the responsible for the onset of the movement, while the frictional forces were in charge of the stopping condition. These experiments, being free from the influence of the topography, were of utmost importance, since they provided results concerning the quantity of mass mobilized by the flow, the final shape and the maximum spreading of the granular mass.

Another important configuration which has been recently mimicked in the laboratory consists of granular flows traveling over erodible topography, (Mangeney et al., 2010; Roche et al., 2011). This phenomena is easily found in nature, as under certain circumstances landslides can move over deposits built up by earlier events. The strong effects of erosion processes can significantly increase the mobility of avalanches, changing drastically the final distribution of the granular mass, (Mangeney-Castelnau et al., 2005; Bouchut et al., 2008; Mangeney et al., 2010).

The study of granular flows in combination with obstacles has also acquired prominence during the last years. The impact of the obstacle in the flow behavior needs to be understood for a better design of civil engineering elements such as mast of electrical power lines, buildings, ski lifts, dams and other man-made structures. Several works have dug on this active research field, some of them analyzing the flow overtopping on dike elements (Hakonardottir et al., 2003; Faug et al., 2008) and other ones focusing on the shock waves generated by the impact between the flow and the single obstacle (Gray et al., 2003; Hakonardottir and Hogg, 2005; Hauksson et al., 2007).

Following the previous effort made by the authors mentioned above (Gray et al., 2003; Hakonardottir et al., 2003; Hakonardottir and Hogg, 2005; Hauksson et al., 2007), the main concern of this work is in relation with the study of the variable nature of the moving shocks and their complex birth and propagation. Since we want to get closer to the phenomenology which takes place in nature, a series of laboratory experiments have been carried out for studying novel an real-life configuration: 2D spread of the granular mass over variable topography with a changing slope and multiple shock waves derived from the presence of multiple obstacles. The experimental avalanche is triggered by a simple mechanism: a granular mass which is suddenly released from a semi-spherical container. The full description of the experimental facility, methods and cases is found in the experimental paper which accompanies the present work. To provide a physical insight into these phenomena, the spatial and temporal spreading dynamics and the morphology of the resulting shape are investigated and discussed in this work through the wave theory (Roe, 1983). This theory is based on solving the Riemann problem and, originally, it was applied to pure hyperbolic systems of equations. As the geophysical flows involve the presence of source terms, in Murillo and García-Navarro (2012); Juez et al. (2013), approximate solvers where developed devoting special attention to the numerical fixes (entropy fix, friction fix and time step fix). In this fashion, the numerical tool obtained provides accurate numerical predictions even in cases of complex topography and with independence of the reference coordinate system employed. Therefore, the computed results generated are free of distorting numerical effects allowing to study the physical features involve in the granular flows.

This work is organized as follows: section 2 is devoted to a brief summary of the laboratory set up where the experiments have been carried out, section 3 describes the mathematical model employed. Section 4 displays briefly the numerical scheme used and in section 5 the computed results are compared with the experimental data, and several geophysical processes are addressed and explained.

2. Experimental setup and results

The experimental setup is briefly addressed in this section as a detailed explanation is provided in the companion paper. The laboratory experiment was carried out on an inclined rough plane with a changing slope and without lateral walls. Three experiments were carried out with this experimental facility. Each of them was defined by a particular obstacle configuration. Experiment 1 consisted of a single semisphere obstacle located on longitudinal axis of the slope. Experiment 2 had the same semisphere obstacle as in the prior experiment but included also two smaller semisphere obstacles positioned upstream. Experiment 3 had a square bar as obstacle across the transversal direction of the slope. The initial condition was the same for the three experiments and consisted of a semispheric cap full of sand at the upstream end of the facility. Sand grain diameters ranged from 1 mm to 2 mm. The granular avalanche was triggered by the sudden release of the semispheric deposit. A schematic representation of the experimental setup is displayed in Figure 1.

Three-dimensional temporal and spatial data of the moving mass was throughly collected. The measurement technique employed included an RGB-D sensor on the top of the experimental facility and a reflex camera which was set up from different views to complete the data.

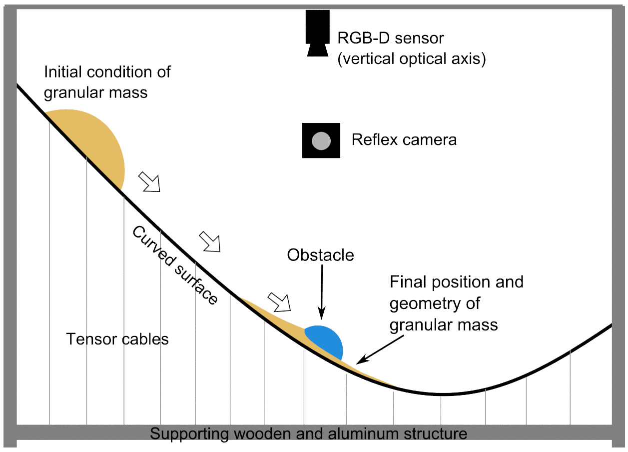

Figure 1: Section 2. Schematic representation of the experimental setup

3. Mathematical model

For the discussion of the observed results, the mathematical model formulated in global coordinates in Juez et al. (2013) is considered. This model for dense granular dry flows without interstitial fluid assumes that the material is oriented in a predominantly longitudinal direction and is confined to a layer which is thin compared to the scale of interest. Hence the depth-averaged procedure is performed in the mass and momentum equations. Hydrostatic pressure distribution in the direction normal to the bed is considered and a Coulomb type bed friction formulation is used to model the basal stress. Additionally, in presence of steep slopes, the gravity vector needs to take into consideration projections derived from bed topography as detailed in Juez et al. (2013). The adequate definition of the fluxes and source terms is an important issue when the bed slopes may change within the domain, since these terms are the responsible of preserving quiescent equilibrium stages and the start/stop flow conditions.

Consequently, the depth averaged equations expressing volume and momentum conservation are written as follows

$$\frac{\partial \mathbf{U}}{\partial t} + \frac{\partial \mathbf{F}(\mathbf{U})}{\partial x} + \frac{\partial \mathbf{G}(\mathbf{U})}{\partial y} = \mathbf{S}_\tau + \mathbf{S}_b \tag{1}$$

where

$$\mathbf{U} = \begin{pmatrix} h, & hu, & hv \end{pmatrix}^T \tag{2}$$

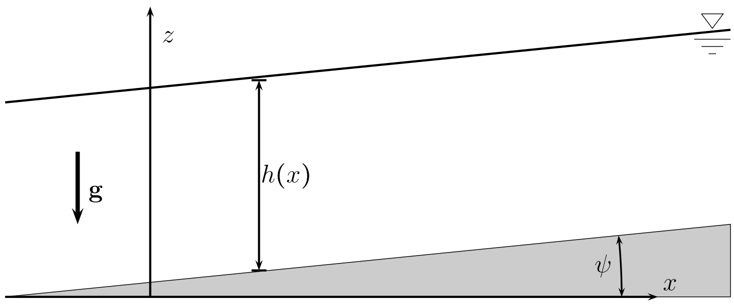

Figure 2: 1D sketch of global coordinates

are the conserved variables, with h representing mass depth in the z coordinate and (u, v) the depth averaged components of the velocity vector along x, y coordinates. The fluxes are given by

$$\begin{aligned} \mathbf{F} &= \left(hu, hu^2 + \frac{1}{2}g_\psi h^2, huv\right)^T \\ \mathbf{G} &= \left(hv, huv, hv^2 + \frac{1}{2}g_\psi h^2\right)^T \end{aligned} \tag{3}$$

where $g_\psi = g\cos^2\psi$, being ψ the direction cosine of the bed normal with respect to vertical, Juez et al. (2013). The term $\mathbf{S}_\tau$ represents the frictional effects in the bed, and is defined as

$$\mathbf{S}_\tau = \left(0, -\frac{\tau_{b,x}}{\rho}, -\frac{\tau_{b,y}}{\rho}\right)^T \tag{4}$$

with $\tau_{b,x}, \tau_{b,y}$ the bed shear stress in the x and y direction respectively and ρ the density of the granular mass.

The term $\mathbf{S}_b$ is defined as

$$\mathbf{S}_b = \left(0,\ -g_\psi h\frac{\partial z}{\partial x}, -g_\psi h\frac{\partial z}{\partial y}\right)^T \tag{5}$$

and expresses the variation of the pressure force in the x and y direction respectively. Figure 2 shows a 1D sketch of the global coordinates and the variables involved in system 2.

Regarding equations (3) and (4) some extra considerations are noteworthy. Regarding the flux terms, the velocity profile across the material layer is assumed to be well modeled as a plug flow, following Pouliquen and Forterre (2002), who stated how changes in the shape of the velocity profile had slight importance in the dynamic of the flow. Moreover, some works (Savage and Hutter, 1989; Gray et al., 1999; Pouliquen and Forterre, 2002; Pirulli et al., 2007) include a coefficient K in the term of the pressure force linked to the thickness gradient, which represents a ratio of the normal horizontal stress (x-y direction) to the normal vertical stress (z direction) Savage and Hutter (1989). This K coefficient is built through the Mohr-Coulomb theory (Savage and Hutter, 1989), which was derived on the basis of a rigid solid. However, since in this type of geophysical flows, the granular material behaves as a fluid, no large differences between vertical and horizontal stresses are present, Ertas et al. (2001); Pouliquen and Forterre (2002). Consequently, in this work, it is not considered.

Focusing on (4), some extra forces may need to be considered. Bouchut et al., Bouchut et al. (2003) introduced a new term in the mathematical model, related to the curvature of the bottom, which is usually neglected when compared in terms of magnitude. However, in some phenomena, such as landslides over large areas, the curvature terms play an important role (Favreau et al., 2010; Moretti et al., 2012). In recent works, Pirulli et al. (2007); Pirulli and Mangeney (2008), this term was omitted and promising computational results were obtained. Following Pirulli et al. (2007) and Pirulli and Mangeney (2008) curvature terms related with the geometry are not included in the mathematical model used herein.

3.1. Empirical friction law

The description of the rheological laws which govern geophysical granular flows is not a trivial task, as it is necessary to delve into their physical origins at the grain scale. The main advantage of the depth averaged equations is precisely, that the dynamics of the flowing layer can be predicted without knowing in detail the internal structure of the flow, (Pouliquen and Forterre, 2008). The complex three dimensional rheology of the granular mass is mainly considered through the basal friction term. Assuming a simple constant Coulomb-like basal friction is generally sufficient to capture the main flow structures and has been widely used to describe granular motion (Pouliquen and Forterre, 2002; Bouchut et al., 2003; Kerswell, 2005; Pirulli et al., 2007; Juez et al., 2013). This basal friction term is governed by a dynamic angle of friction which is usually several degrees less than the traditional static friction angle (Cui and Gray, 2013).

However, when considering complex transient situations which involve realistic topography and propagating shocks, more sophisticated basal friction laws may need to be considered. The assumed dense quasi-static regime may fail and an intermediate liquid regime can develop in which the collision forces take center stage. In the search of accurate quantitative predictions several authors (Pouliquen and Forterre, 2002; Forterre and Pouliquen, 2003; Pirulli et al., 2007) have studied in detail the onset and overall behavior of the gravity-driven flows. As it was stated in Pouliquen (1999); Pouliquen and Forterre (2002), experimental works have proved the existence of two critical angles: an initial static angle which governs the onset of the movement, θ_{start}, and another lower angle, which is in charge of the stopping phenomena, θ_{stop}. A relationship between both angles can be found in Pouliquen and Forterre (2002), providing a way of explaining the hysteresis behavior of granular slope stability (Douady et al., 1999). Additionally, Da Cruz et al. (2005) discussed another way of computing the friction coefficient in terms of the relevant timescales controlling grain motion (mean deformation and confining pressure). Both approaches, Pouliquen and Forterre (2002); Da Cruz et al. (2005), despite of providing a full description of the granular behavior at different regimes present the main drawback of requiring ad hoc parameters. In this way, the accuracy of the predictions are tied to the accuracy of the calibration which is usually supplied by small-scales laboratory test.

In order to avoid these calibration parameters, but pursuing a more sophisticated friction term not only a dry friction law is considered in this work. Regarding the fact that the conservation equations in (1) are depth averaged, the tangential forces generated by the stresses may have different and wide nature: turbulent stress τ_t, dispersive stress τ_d, Coulomb-type frictional stress τ_f, yield stress τ_y and even viscous stress τ_μ. Not all stresses act along or simultaneously at the same location of the material column. However, since the conceptual model is depth-averaged, all terms may actually coexist and may be mathematically lumped in the same formula. For this reason, and because the mathematical structure of the equations is the same as the one of the shallow-water equations, and following previous works (Johnson and Jackson, 1987; Louge, 2003; Hungr and McDougall, 2009), the Manning's law (Manning, 1895) is considered in addition to the dry frictional Coulomb's law.

The Manning's law is based on a power-law velocity model where the friction exerted over the bed is written as the product of a friction coefficient and the square velocity profile. Depth averaging this expression and considering turbulent flow on the basis of the flow, (Burguete et al., 2007), drives to define the new tangential forces as

$$\begin{aligned}\tau_{t,x} &= \rho g_{\psi}\tfrac{n^2 u\sqrt{u^2+v^2}}{h^{1/3}}\\ \tau_{t,y} &= \rho g_{\psi}\tfrac{n^2 v\sqrt{u^2+v^2}}{h^{1/3}}\end{aligned} \tag{6}$$

where n is the Manning-Strickler's coefficient which is related to the bed topography roughness. With the inclusion of this friction term in the momentum equations, the effect of very thin layers where only a small number of grains are present in the vertical column is taken into account (the collisional term becomes more relevant). Since under these conditions only few layers of granular material exist, and all of them are mobilized, the local dissipation of the potential energy needs to be increased in such area. In this fashion, the stopping conditions of the moving mass is not only reached when the slope of the surface level equals the slope of the friction angle. Thanks to the mathematical structure of Manning's law, the smaller the granular depth is, more friction dissipation is generated at the base of the flow. Hence, the sum of tangential forces of (4) applied over the moving mass are evaluated as

$$\begin{aligned}\tau_{b,x} = \tau_{f,x} + \tau_{t,x} \quad i.e. \quad \tau_{b,x} = \rho g_{\psi} h\tan\theta_b + \rho g_{\psi}\tfrac{n^2 u\sqrt{u^2+v^2}}{h^{1/3}}\\ \tau_{b,y} = \tau_{f,y} + \tau_{t,y} \quad i.e. \quad \tau_{b,y} = \rho g_{\psi} h\tan\theta_b + \rho g_{\psi}\tfrac{n^2 v\sqrt{u^2+v^2}}{h^{1/3}}\end{aligned} \tag{7}$$

4. Numerical scheme

System (1) is solved through the numerical scheme for global coordinates proposed in Juez et al. (2013) which is based on a Finite Volume Model. System (1) is integrated in a grid cell Ω_i

$$\frac{\partial}{\partial t}\int_{\Omega}\mathbf{U}d\Omega + \int_{\Omega}(\overrightarrow{\nabla}\mathbf{E})d\Omega = \int_{\Omega}\mathbf{S}d\Omega \tag{8}$$

Using Gauss theorem (8) is written as

$$\frac{\partial}{\partial t}\int_{\Omega_i}\mathbf{U}d\Omega + \oint_{\partial\Omega_i}\mathbf{E}_{\mathbf{n}}dl = \int_{\Omega_i}\mathbf{S}d\Omega \tag{9}$$

where vector $\mathbf{n}$ is outward from cell Ω_i, as displayed in Figure 3. The second integral in (9) can be explicitly expressed as a sum over the cell edges,

$$\frac{\partial}{\partial t}\int_{\Omega_i}\mathbf{U}d\Omega + \sum_{k=1}^{NE}\int \mathbf{E}_{\mathbf{n}k}dl_k = \int_{\Omega}\mathbf{S}d\Omega_i \tag{10}$$

with $\mathbf{n}_k = (n_x, n_y)$ the outward unit normal vector to the cell edge k, dl_k is aligned in the direction of the edge and NE is the number of edges in cell i, as shown in Figure 3.

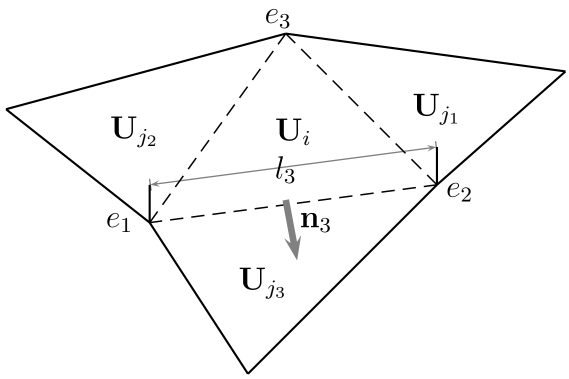

Figure 3: Cell parameters

Assuming a first order in space approach, (10) becomes

$$\frac{\partial}{\partial t}\int_{\Omega_i} \mathbf{U} d\Omega + \sum_{k=1}^{NE} \mathbf{E_n}_k l_k = \int_{\Omega} \mathbf{S} d\Omega_i \tag{11}$$

Also, the volume integrals of the source terms are expressed in terms of appropriate contour integrals by projecting the source terms onto the normal direction $\mathbf{n}_k$ to each cell edge as follows

$$\int_{\Omega_i} \mathbf{S} d\Omega_i \approx \sum_{k=1}^{NE} \int_{x'} \left[\mathbf{S}_k dx'_k\right] l_k \tag{12}$$

being x' the coordinate normal to cell edge k, as shown in Figure 4. Then, the initial system of equations in (1) is transformed in

$$\frac{\partial}{\partial t}\int_{\Omega_i} \mathbf{U} d\Omega + \sum_{k=1}^{NE} \left(\mathbf{E_n} - \int_{x'} \mathbf{S}_k dx'\right)_k l_k = 0 \tag{13}$$

System (13) is solved using approximate linear solutions of initial value problems according to the Godunov method, where $\mathbf{U}_i^n$ is the cell-average value of the solution $\mathbf{U}(x, y, t)$ for the ith cell at time t^n

$$\mathbf{U}_i^n = \frac{1}{A_i}\int_{\Omega_i} \mathbf{U}(x, y, t^n) d\Omega \tag{14}$$

being A_i the cell area. Assuming a piecewise representation of the variables within the cell drives to define an uniform value for each variable.

The development of the numerical scheme in the Godunov method can be completed by the definition of an approximate solver of the Riemann problem, hereafter RP, governed by the fluxes at each side of each edge, $\mathbf{E}_j$ and $\mathbf{E}_i$. For the Roe's approximate solver this solution is given by an approximate Jacobian matrix constructed through the flux difference $(\delta\mathbf{E})_k = \mathbf{E}_j - \mathbf{E}_i$, Roe (1983).

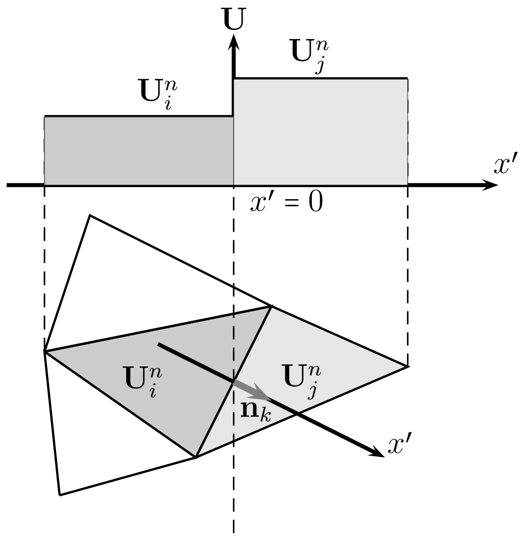

Figure 4: Riemann problem in 2D along the normal direction to a cell side

As it was justified in Juez et al. (2013) the piecewise representation of the variables in the Godunov method and the definition of gravity forces affected by the presence of non-uniform topography are need to bring together to ensure the well-balanced property at each RP. Following Juez et al. (2013), appropriate integrals for the bed slope and friction terms are provided and through the upwinding technique the variables are spatially and temporally updated. The allowable time step size are controlled by the CFL condition (Murillo and García-Navarro, 2012).

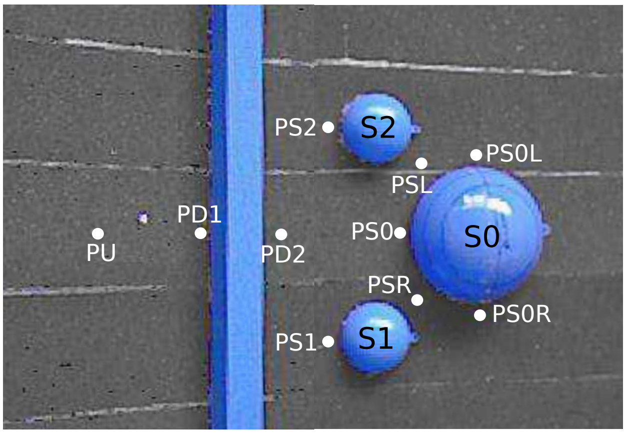

Figure 5: Section 5. Probes location

5. Results and discussion

The purpose of this section is twofold: first, we aim to validate the computed results obtained by comparison against the experimental data. Therefore, the forecasting capabilities of the shock-capturing scheme are explored when considering a fast 2D transient condition with a variable topography which includes obstacles. Additionally, a discussion on the physics involved in the granular flow behavior is developed. Some fluid-mechanical characteristics are identified, providing useful information for future design guidelines of dikes or other man-made civil elements.

All the simulations have been performed using an unstructured Delaunay triangular mesh, since only this type of mesh avoids the presence of misleading preferential flow directions as shown by Juez et al. (2013). A maximum cell area of 6 mm^2 is considered with a stability condition of CFL = 0.4. The bed domain is considered non-deformable and no boundary conditions are imposed.

Comparisons between experimental and computational results are based on quantitative temporal 3D information detailed in companion paper. 2D plan views and a number of probes located at points of interest, shown in Table 5, are analyzed in depth. A summary of all the probes is presented in Figure 5.

Probe	X (mm)	Y (mm)
PU	500	500
PD1	600	500
PD2	680	500
PS0	760	500
PS1	705	410
PS2	705	590
PSL	770	550
PSR	770	450
PS0L	814	570
PS0R	814	430

Table 1: Probe locations

5.1. Gravity driven flow facing up a single obstacle

The understanding of the flow behavior against obstacles gathers a great interest as it is crucial in the design of elements which protect civil buildings and structures from several types of material slides (snow avalanches, debris flows, rockfalls or pyroclastic flows). Prior works have also pointed out the importance of this kind of configuration, carrying out 1D laboratory experiments with cylindrical obstacles Gray et al. (2003); Cui and Gray (2013) and with square blocks Hauksson et al. (2007). Being conscious that a landslide is a genuinely 2D flow, although under particular circumstances it can be constrained by bed topography driving to a 1D flow, we have developed a 2D experimental case as in Tai et al. (2001) but over a rough bed surface. For this purpose, in the experiment considered in this subsection a single obstacle with semispherical shape is located within the flow region. This semisphere can be seen as an obstacle and also as a characteristic of the bed topography. Figure 6 shows a three-dimensional plot of the initial configuration.

Before comparing computed results with the experimental data, the influence of the dynamical friction angle and the effect of the Manning's term is studied. For this purpose numerical results obtained by using two different dynamical angles, $\theta_b = 22^o$ and $\theta_b = 30^o$ are shown in Figure 7 at the final stage of the experiment. As it is observed, when using $\theta_b = 22^o$ the friction term is diminished in comparison to the inertia terms and the granular mass exceeds the obstacle, which results in two symmetric sand deposits downwards. On the other hand, when applying $\theta_b = 30^o$, the flow is stopped

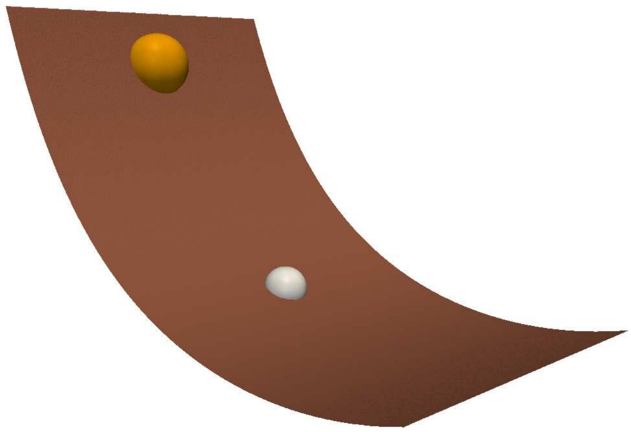

Figure 6: Section 5.1. Initial configuration with the sand deposit at the beginning of the slope and the obstacle downwards

before overrunning the obstacle.

Additionally, the effect of the gravity projections considered in the numerical scheme is also analyzed. For this purpose, Figure 8 displays the final stage with two different dynamical angles, $\theta_b = 22^o$ and $\theta_b = 30^o$ and without considering the projections. As it observed, the overall surface level is completely different from Figure 7 and an important mismatch of a physically-based behavior is observed. Therefore, the effect of the gravity projections is need it is retained from now on in all the computed results.

Bearing in mind the granular movement observed in the experiments, more accurate results are obtained when using an intermediate dynamical angle equal to $\theta_b = 26^o$, Figure 9 (a). Once the effect of the dynamical angle is clearly identified, the effect of Manning's law is taken into account in the friction term. In this fashion, the final stage of the granular avalanche, shown in Figure 9 (b), displays some differences with respect to 9(a): the front of the avalanche keeps the same maximum spreading and the lateral movement is almost identical. However, noticeable discrepancies appear in the tail of the avalanche: whereas with the unique existence of the friction angle the effects of the thin layer are not taken into consideration and the tail is shortened, when considering the Manning's law the tail is enlarged, providing a better physical description of the phenomena.

A temporal sequence of 3D views, numerically obtained, is plotted in Figure 10. Additionally, in Figures 12 and 13 a temporal series of 2D plan views with experimental data and computational results are presented. Since

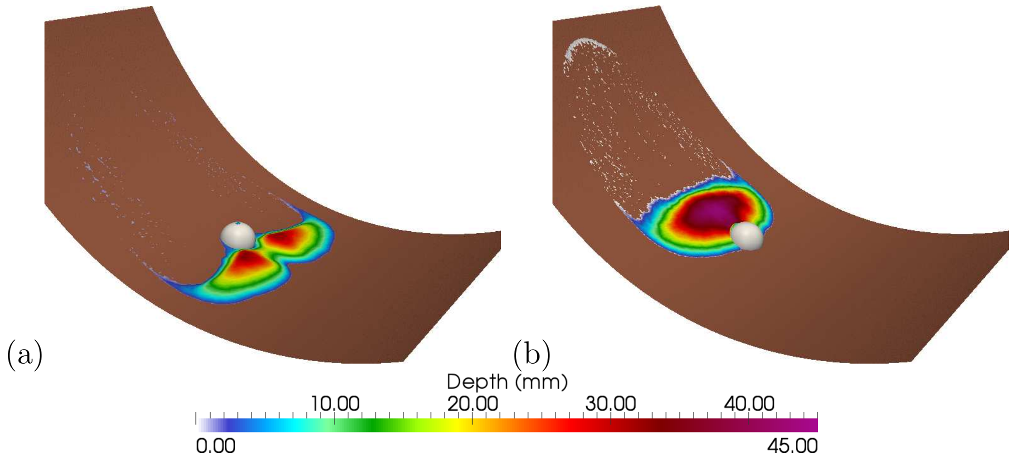

Figure 7: Section 5.1. Final stage of the granular avalanche with two different dynamical friction angles $\theta_b = 22^o$ (a) and $\theta_b = 30^o$ (b) at the final stage of the movement

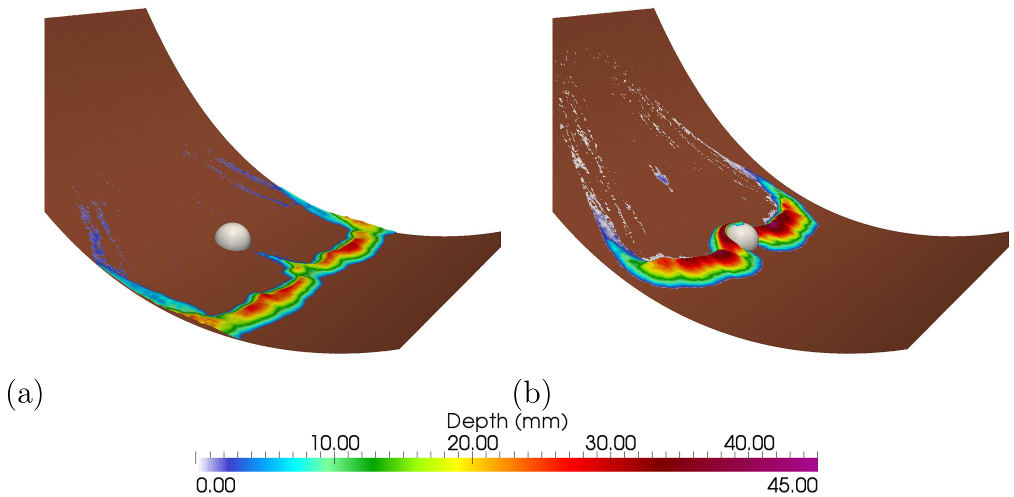

Figure 8: Section 5.1. Final stage of the granular avalanche with two different dynamical friction angles $\theta_b = 22^o$ (a) and $\theta_b = 30^o$ (b) and without considering the gravity projections at the final stage of the movement

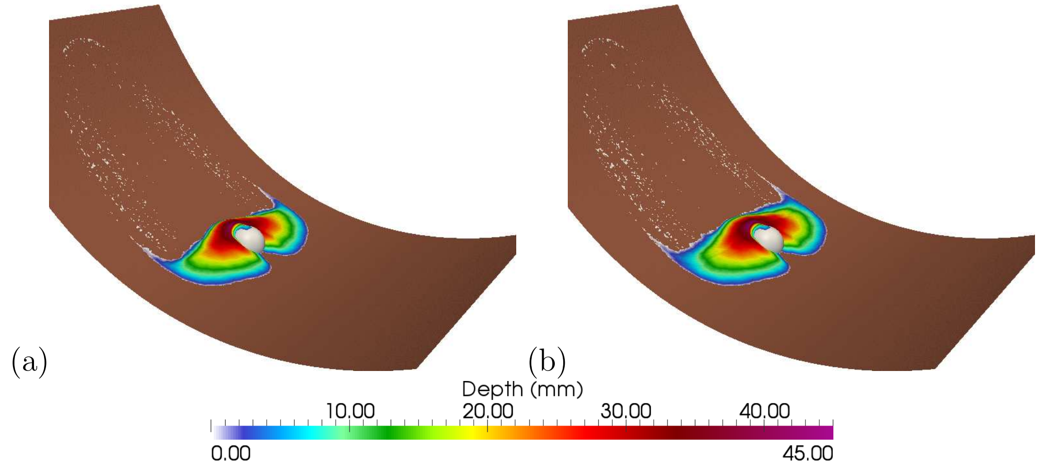

Figure 9: Section 5.1. Final stage of the granular avalanche when using only the dynamical friction angle with $\theta_b = 26^o$ (a) and when summing the Manning's law (b) at the final stage of the movement

the sand cap is suddenly removed, the overall granular mass is put in motion and the initial shape is lost quickly. The flow spreads over the longitudinal and transversal direction until it reaches the obstacle, at $t = 540\,ms$. At this point, two interesting flow structures are formed: a wake region downslope from the semisphere, and a shock region upstream and to the sides of the semisphere. The shock evolves symmetrically around the sphere until the avalanche front remains at rest at $t = 1000\,ms$. From this temporal point, only the granular tail is still in motion up to an equilibrium stage at $t = 2000\,ms$. An important phenomena reported in the companion work is the existence of a stagnation area, i.e. an area where the granular mass has a local zero velocity. This structure is also observed in the computational results in figure 11, and is temporally well described as it occurs at the same time, $t = 850\,ms$, as it was observed in the laboratory. From a numerical point of view, it is remarkable the robustness of the computed solution in the wet/dry fronts: the computed solution is able to handle with these situations without ruining the stability of the numerical solution. This characteristic is of utmost importance since it is present during the movement of the granular mass and when impacting against the obstacle: a part of the sand arrives to the top of the semispheric cap.

When analyzing the numerical results against the experimental data, the overall behavior of the granular mass is well described. Temporal evolution

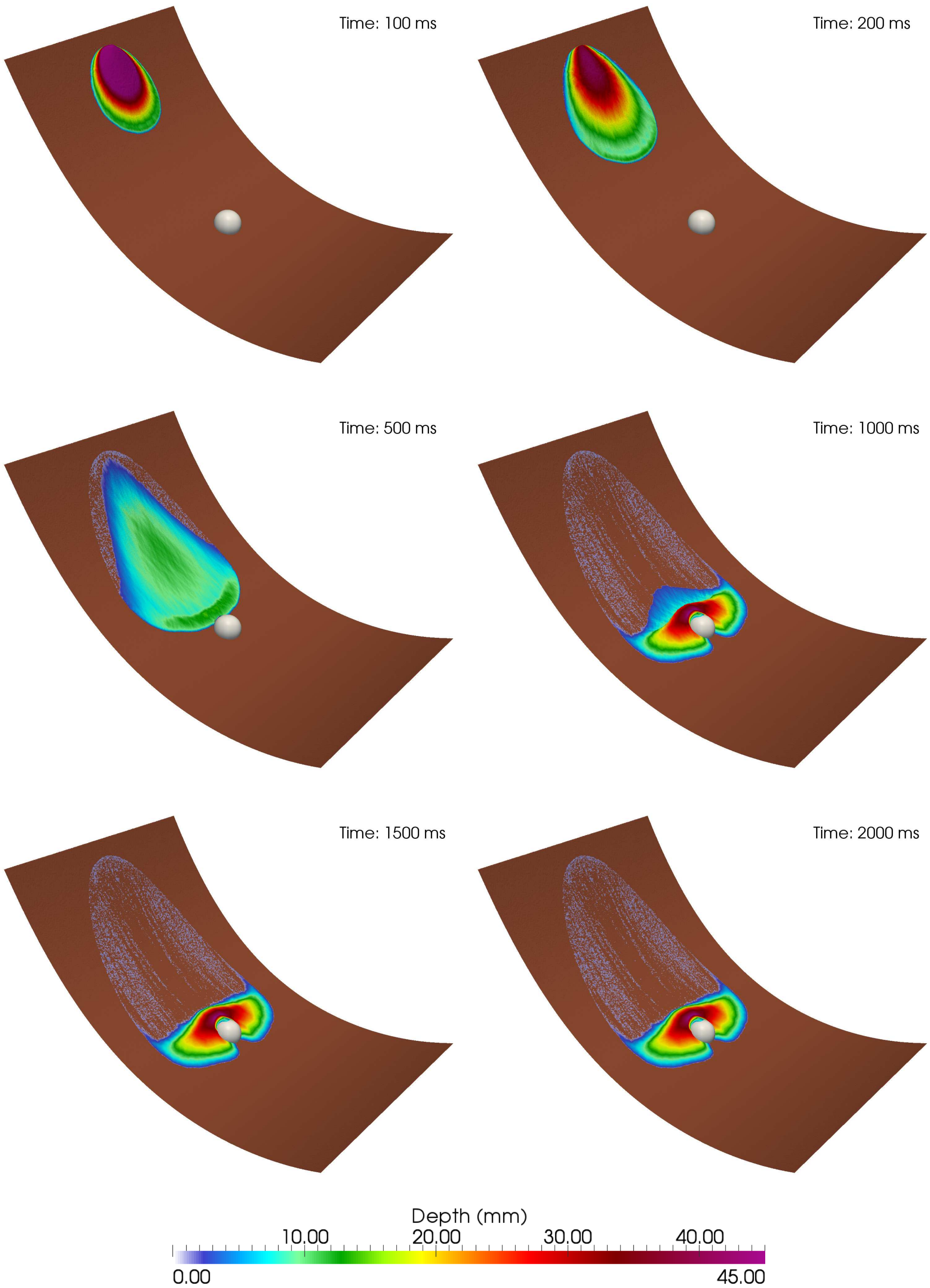

Figure 10: Section 5.1. 3D contour views for the free surface level at times t = 100 ms, t = 200 ms, t = 500 ms, t = 1000 ms, t = 1500 ms and t = 2000 ms

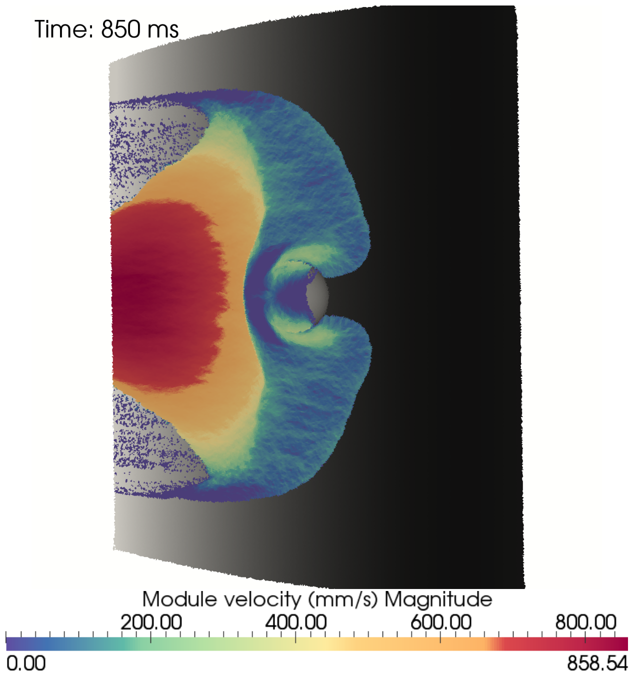

Figure 11: Section 5.1. 2D plant view of the computed velocity field at time $t = 850$ ms

of the sand run out is accurately tracked in time. Furthermore, although the shock is a genuinely 3D structure, it is well reproduced by the depth averaged model considered in this work. However, some differences appear around the shocks area and at the final stage, where the computed results tend to overestimate the sand depth in the vicinity of the semisphere. Both situations are explained by the fact that the mass located in the avalanche tail is not stopped at the adequate position by the numerical scheme. Hence, an extra quantity of mass evolves downslope increasing the sand depth up to reach a rest condition. This fact is clearly understood when computing the absolute error between numerical and experimental results, Figure 14. Red areas, located at the sides of the obstacle showed a higher prediction for the sand depth, whereas the blue areas positioned at the avalanche tail show an underestimation of the mass. Nevertheless, the error at the avalanche front is close to zero, which implies an accurate tracking of the transient moving mass.

All the probes measured in the companion work (except PU, which in this experiment was not recorded) are compared with the computed results, Fig-

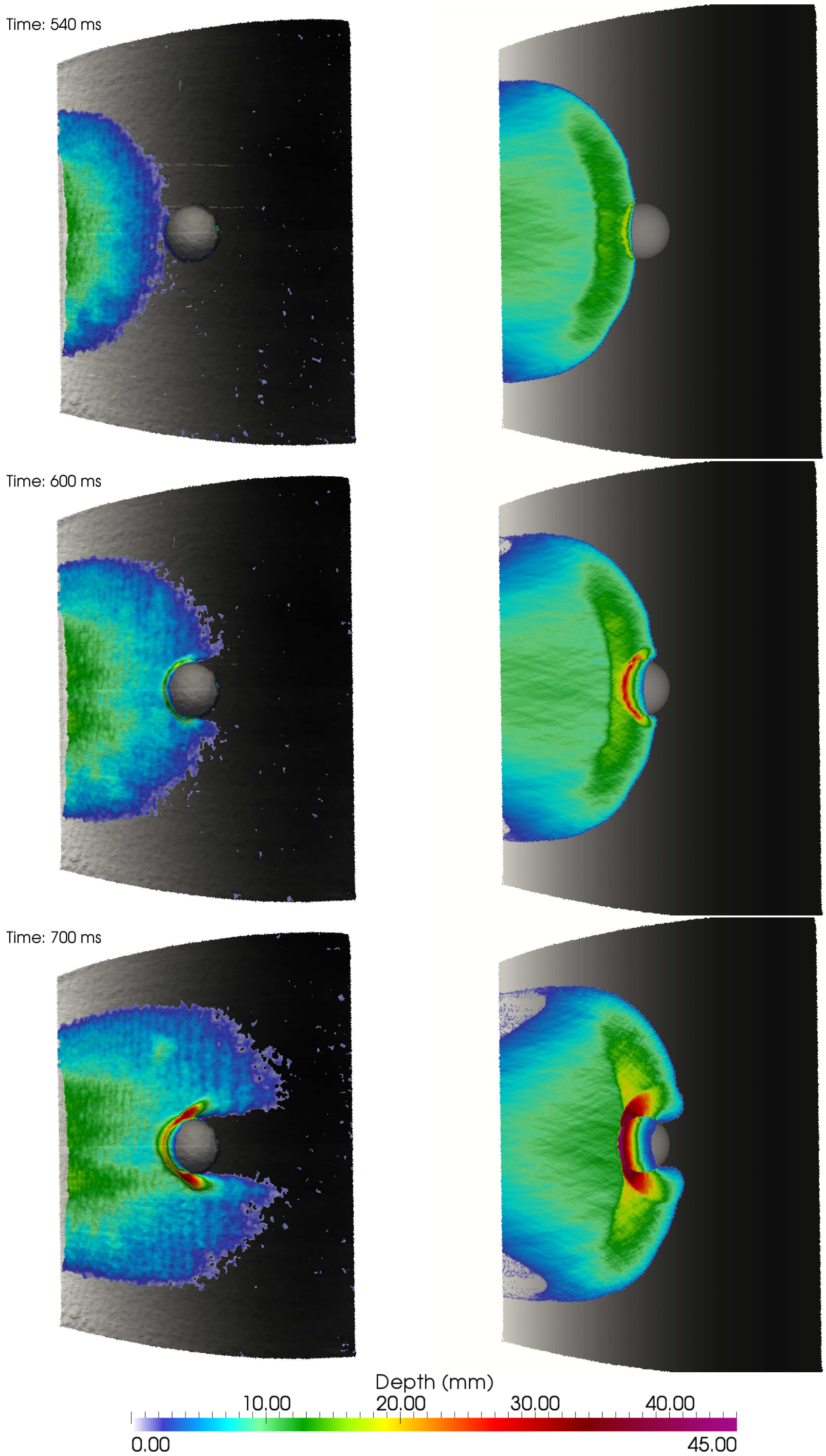

Figure 12: Section 5.1. 2D plant views for the sand depth obtained experimentally (left side) and computationally (right side) at times $t = 540$ ms, $t = 600$ ms, $t = 700$ ms

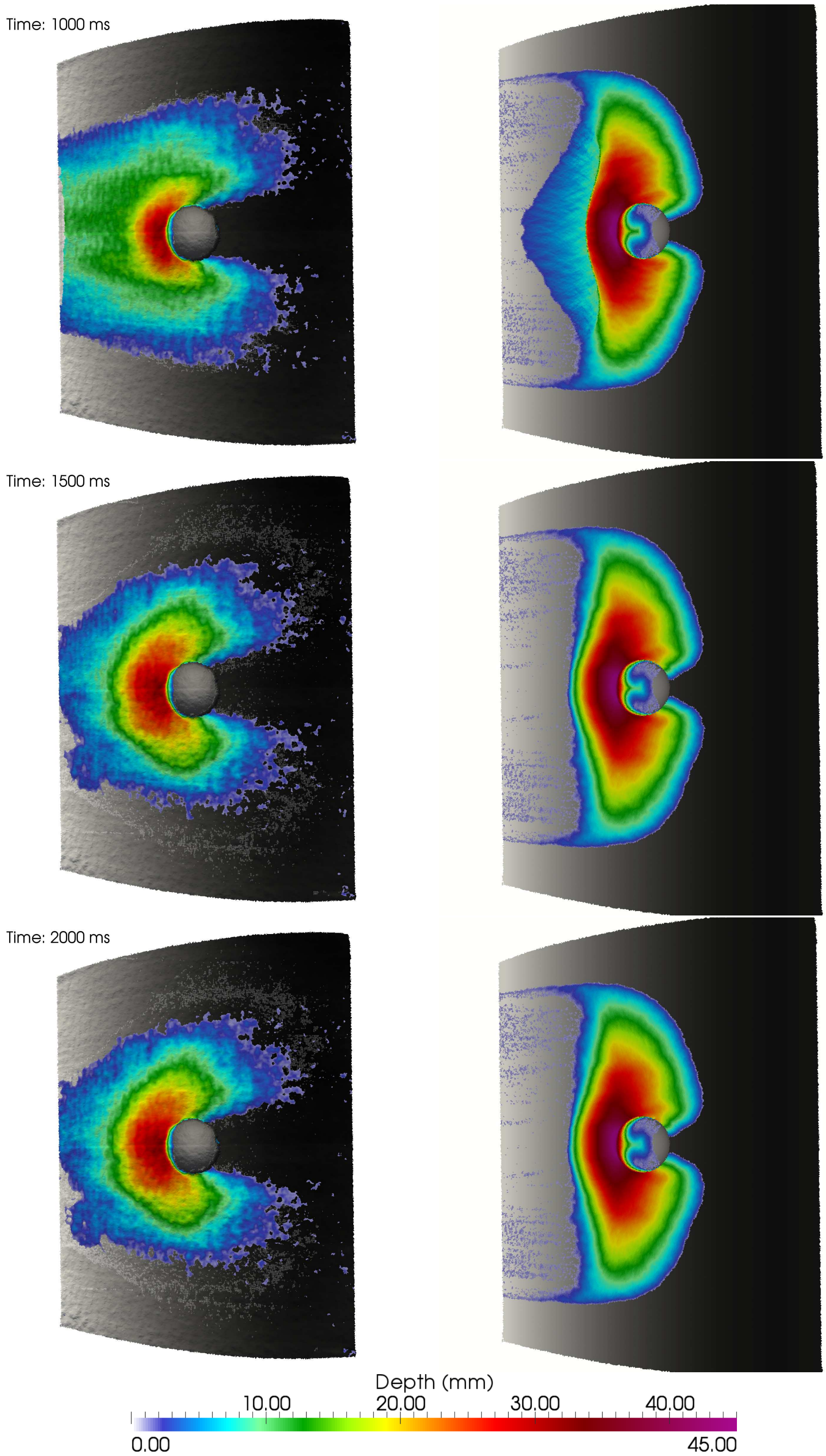

Figure 13: Section 5.1. 2D plant views for the sand depth obtained experimentally (left side) and computationally (right side) at times $t = 1000$ ms, $t = 1500$ ms, $t = 2000$ ms

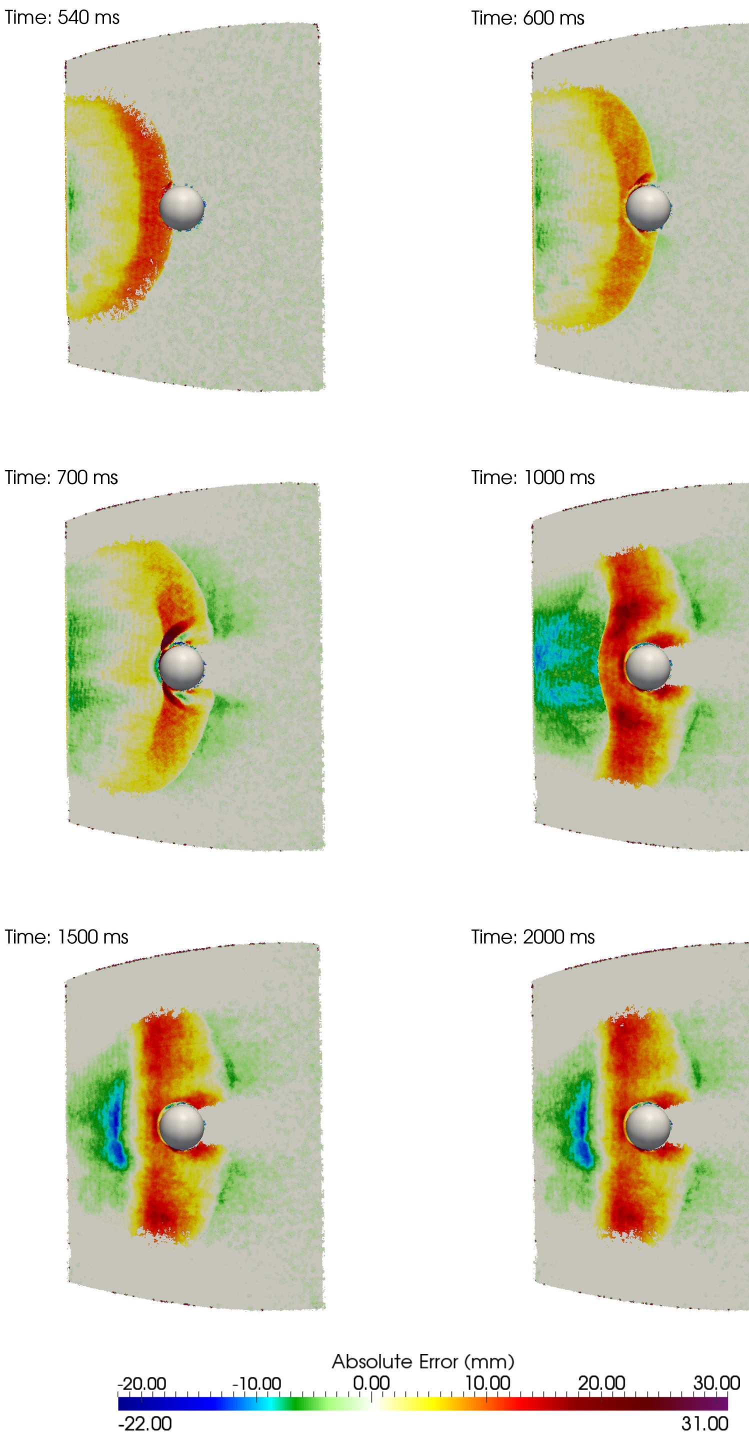

Figure 14: Section 5.1. 2D plant views displaying the absolute error at times $t = 540$ ms, $t = 600$ ms, $t = 700$ ms, $t = 1000$ ms, $t = 1500$ ms, $t = 2000$ ms

ure 15. PD1 shows a time lag with respect to the experimental measurement. This is due to the fact that, during the experiment, the opening of the sand container was not instantaneous, in contrast to the computational assumption under which a sudden dam break of the initial sand cap is considered. Additionally, differences between experimental and numerical results are observed from time $t = 1100\,ms$ and are associated to the different behavior of the avalanche tail observed with the experimental and computed results: in the laboratory work the tail area is spatially stopped before and consequently, the sand depth is stretched. In PD2, which is located downstream from PD1, the time lag perturbation of the gate is less evident. Numerical results are in good agreement with experimental data. An interesting phenomena is observed in the computational solution: the sand depth grows quickly up to time $t = 750\,ms$, then drops up to time $t = 1100\,ms$ and then the sand layer is increased again. Since the avalanche front moves quickly, the granular mass is split into two regions: the front and the tail. Once the front remains at rest, the tail is still in motion and goes on traveling downslope. Therefore, the final height of the sand layer at point PD2 is the sum of two moving masses: first the front and then the tail. PS1 and PS2 provide an accurate prediction of the sand flow and the same explanations given for the jump in the sand depth at PD2 is applicable here. PSL, PSR, PS0L, PS0R, PS0 are placed in the vicinity of the obstacle, providing information of the shocks upstream and to the sides of the semisphere. All of them tracked accurately the temporal evolution. Nevertheless, the final sand depth is overestimated as a consequence of the extra granular mass which comes from the tail area.

In addition to the probes, in Figure 16 a longitudinal profile at $y = 500\,mm$ is shown. The tendency of the experimental measurement is well reproduced by the computed solution, although the predicted surface level is overestimated over the obstacle. This larger amount of material located in the front of the avalanche comes from the tail area. The gap between the numerical results and the experimental data has its origin in the interplay between rheology and deposition processes. The better results provided by the friction law are biased in this case by the absence of a deposition/entrainment condition in the depth-averaged mathematical model (Faug et al., 2004; Tai and Kuo, 2008).

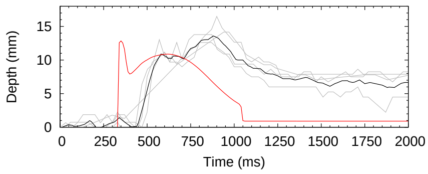

(a) PD1

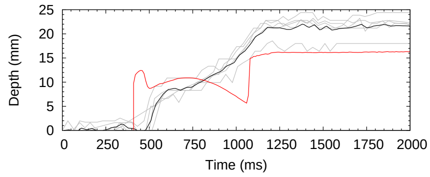

(b) PD2

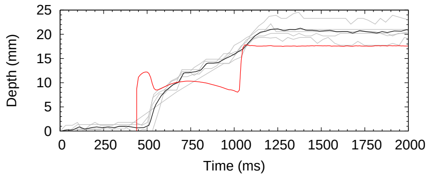

(c) PS1

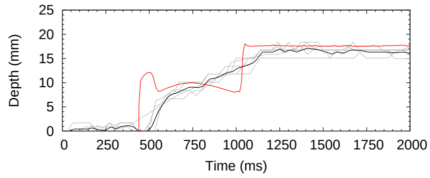

(d) PS2

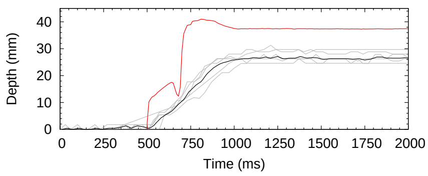

(e) PSL

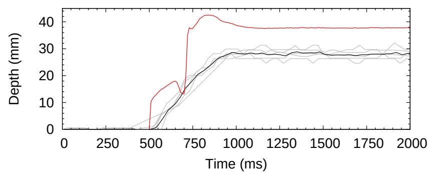

(f) PSR

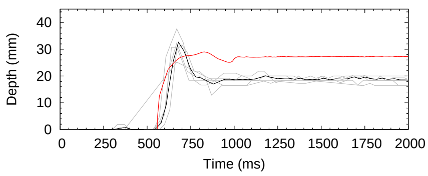

(g) PS0L

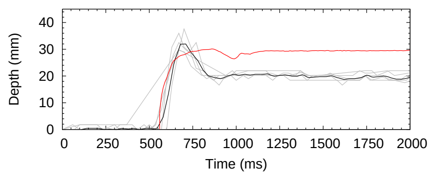

(h) PS0R

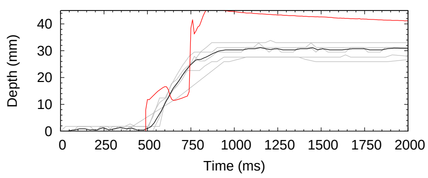

(i) PS0

Exp. repetitions   Exp. Average   Simulated

Figure 15: Computational and experimental probe results

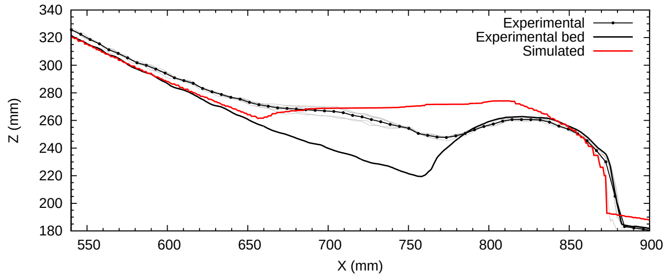

Figure 16: Section 5.1. Longitudinal section ($y = 500\,mm$) for Experiment 1 at the final stage

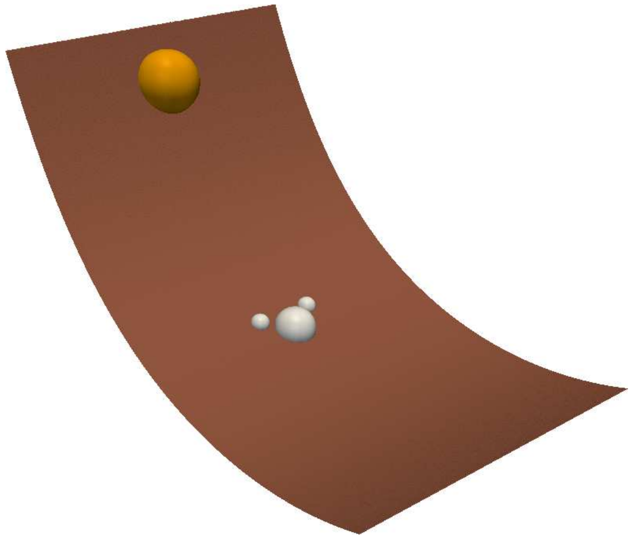

Figure 17: Section 5.2. Initial configuration with the sand deposit at the beginning of the slope and the three obstacle downwards

5.2. Gravity driven flow facing up three obstacles

The next step in this work is considering a configuration which involves several obstacles. In this situation the shock propagation is expected to be influenced by the presence of other moving waves in their vicinity. To our knowledge, this particular configuration has not been addressed in other works. Figure 17 displays a sketch of the initial configuration of the experiment.

The temporal computed evolution of the mass spreading is plotted in 3D and 2D plan views in Figures 18, 20, 21. The first instants of time, prior to the sand reaching the obstacles, are similar to the ones obtained in the experiment with one obstacle. The abrupt opening of the sand container triggers the sand avalanche. The mass is accelerated rapidly downslope towards the obstacles. Both lateral and longitudinal spreadings are observed. The impact of the sand flow against the small semispheres is accurately tracked by the numerical model at time $t = 460\,ms$. At this point the flow undergoes an abrupt transition in flow regimes, since a shock is derived in front of each obstacle at time $t = 640\,ms$ and $t = 740\,ms$. In the vicinity of the shocks the horizontal scales of the phenomena no longer exceed the vertical scales, which constitute a challenge for the shallow approach. Despite the complexity, the computed results describe correctly this complex wave structure, which is generated by the interactions of each obstacle. It is worth noting how the waves numerically reproduced in this experiment, are significantly influenced among themselves. On the other hand, once the flow overtakes the three obstacles, the maximum runout is quickly reached and at time $t = 1500\,ms$ the quiescent equilibrium stage is already achieved. The final shape of the computational results is similar to the obtained in the previous experiment. However, when analyzing the experimental results, it is observed how the surface angle described by the particles in the avalanche front is larger in the three obstacles configuration. With this latter configuration the shocks developed have significantly more influence in the flow behavior and make the sand grains move not only by rolling, but also by salting. This grain mechanism of movement is not affordable with the model proposed in this work and such behavior can not be mimicked.

On the other hand, it is interesting to observe how the numerical results are able to reproduce the initial immersion of the small caps by the sand mass, time $t = 640\,ms$, and the later reappearance of the obstacles, time $t = 1500\,ms$. Furthermore, the stagnation area pointed out in the laboratory work at time $t = 900\,ms$ is also well reproduced with the simulated results, Figure 19.

The main differences between computational and experimental data are due to the overestimated lateral spreading and by the fact that the mass located in the avalanche tail is not adequately stopped. Figure 22 displays the absolute error and the major differences are found in the lateral sides, the vicinity of the obstacles and the avalanche tail. This behavior is fairly similar to the observed in the previous experiment.

The temporal accuracy of the computed results at particular locations during the development of the sand avalanche is validated against the measurements developed during the laboratory work at particular locations as it is described in the companion work. Figure 23 displays all probes plotted in Figure 5 except PU which is out of the field of view in this experiment. The overall behavior of all the probes is similar to the one observed during the experiment with one obstacle. The probes located closer to the sand container, PD1 and PD2, are influenced by the sand release procedure, since, from the computational point of view it is instantaneous, but experimentally it takes a short period of time. This fact provokes a time lag between laboratory data and numerical results. The differences at probes PS1 and PS2 are generated by the numerical behavior of the avalanche: the moving mass is split into two groups: the front and the tail. The tail spreads faster during the first instants of time and consequently, it achieves the equilibrium stage earlier. Then, the mass coming from the tail arrives and the final depth elevation is increased. This phenomena is also responsible for the higher computational sand elevation at probes PSL, PSR, PS0L and PS0R. Nevertheless, the numerical results are able to well reproduce the temporal evolution of this particular avalanche which includes complex transient and local 3D shocks.

Figure 24 displays a longitudinal profile located at $y = 500\,mm$. The overestimated computational sand depth is due to the differences in the tail of the avalanche, where a larger downwards mobilization of the material has occurred. Notwithstanding, the numerical prediction is able to reproduce the fact the the main obstacle is not overtopped.

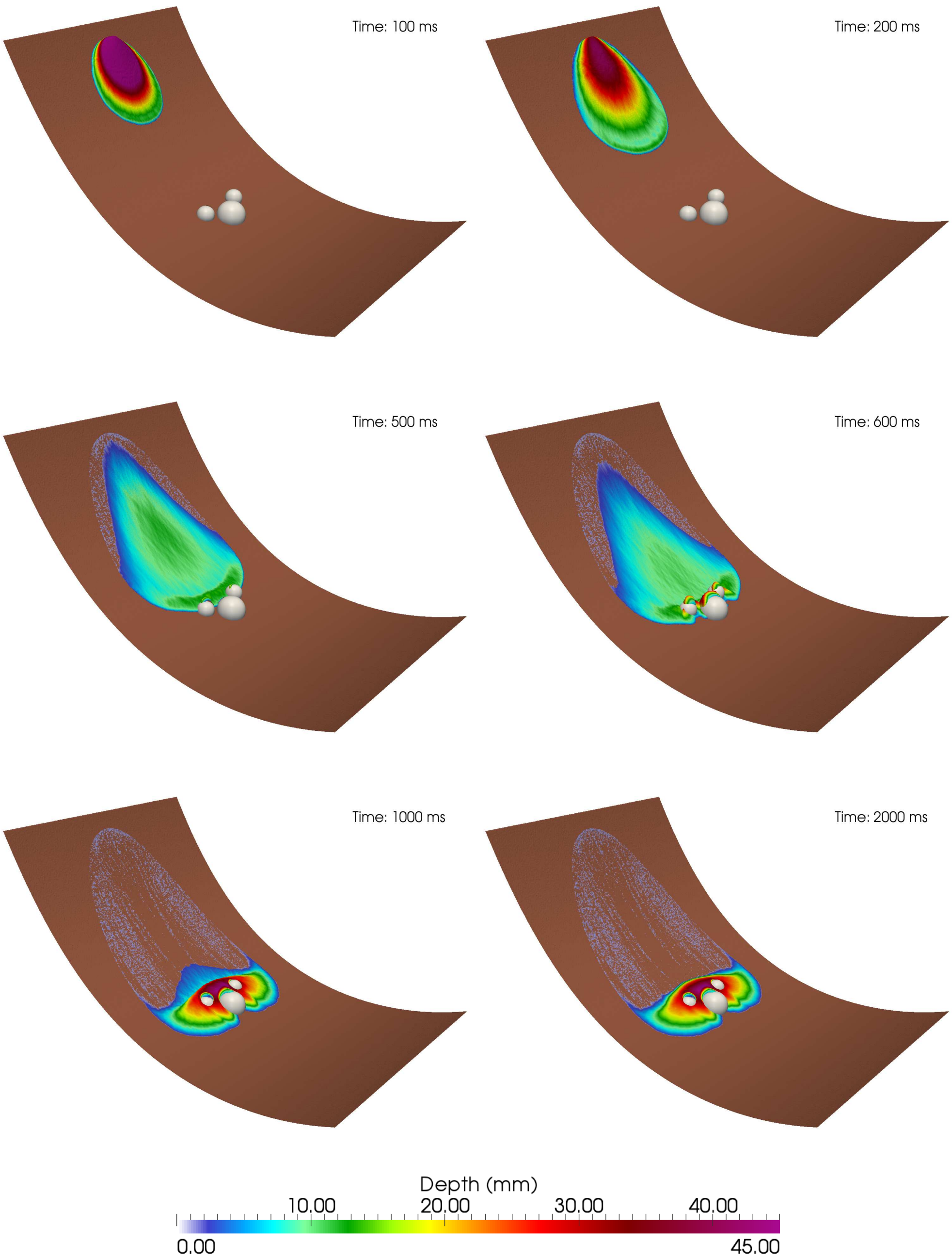

Figure 18: Section 5.2. 3D contour views for the free surface level at times t = 100 ms, t = 200 ms, t = 500 ms, t = 600 ms, t = 1000 ms and t = 1500 ms

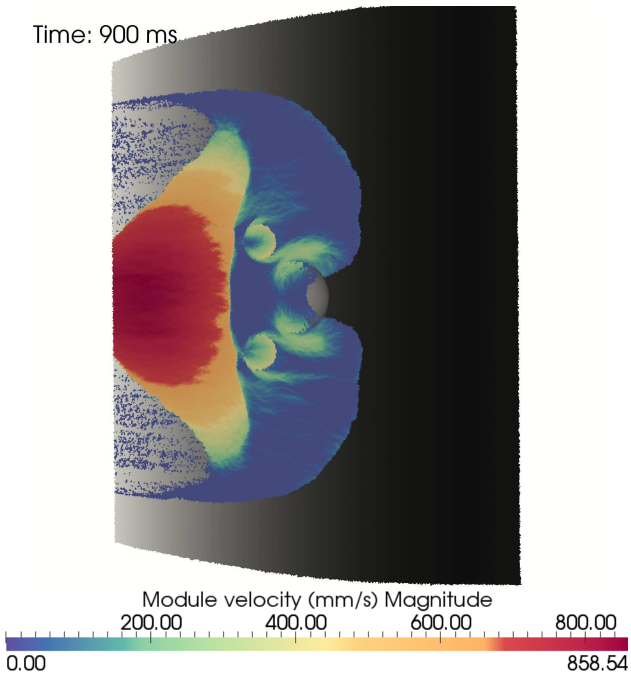

Figure 19: Section 5.2. 2D plant view of the computed velocity field at time t = 900 ms

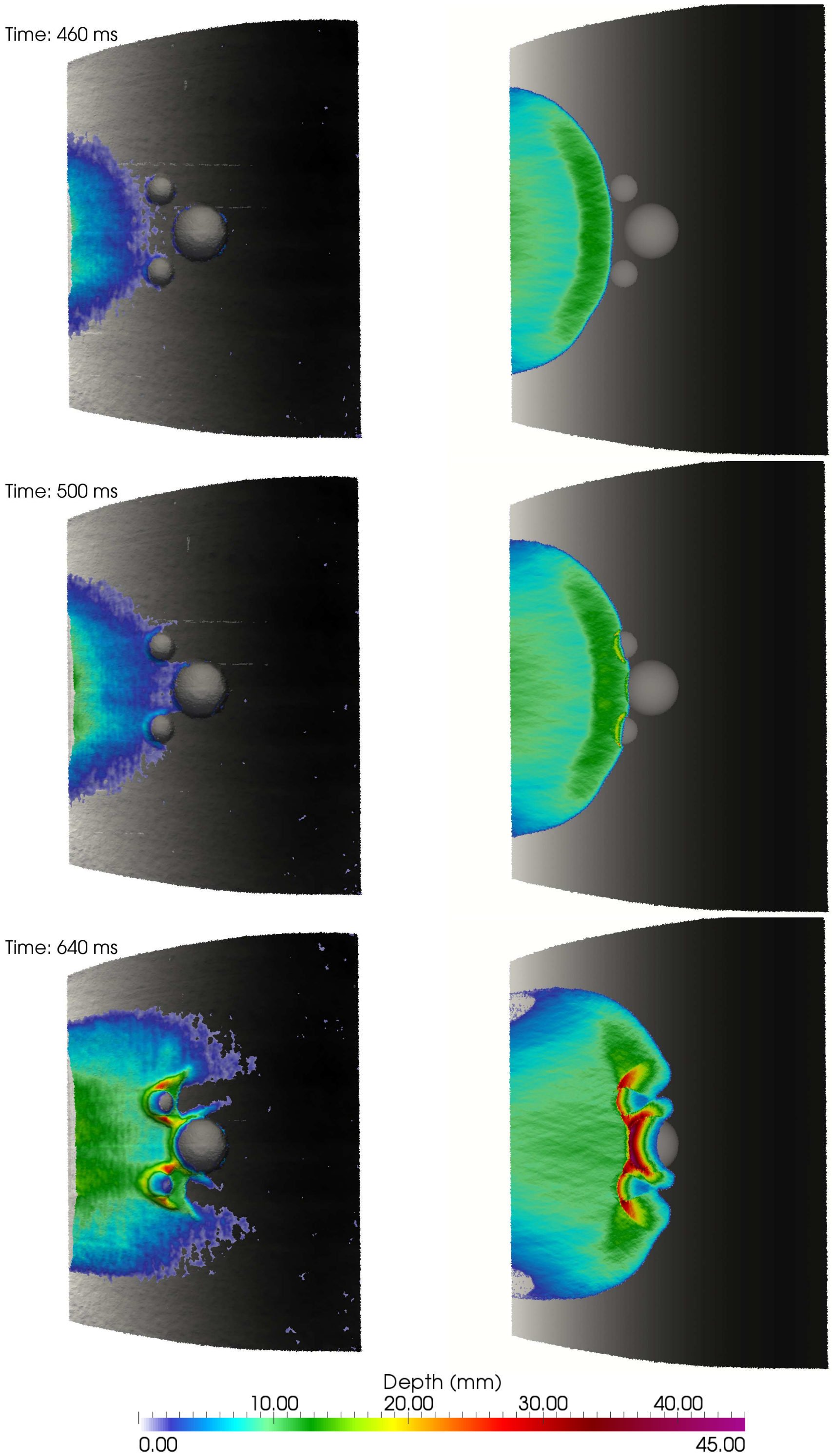

Figure 20: Section 5.2. 2D plant views for the sand depth obtained experimentally (left side) and computationally (right side) at times $t = 460$ ms, $t = 500$ ms, $t = 640$ ms

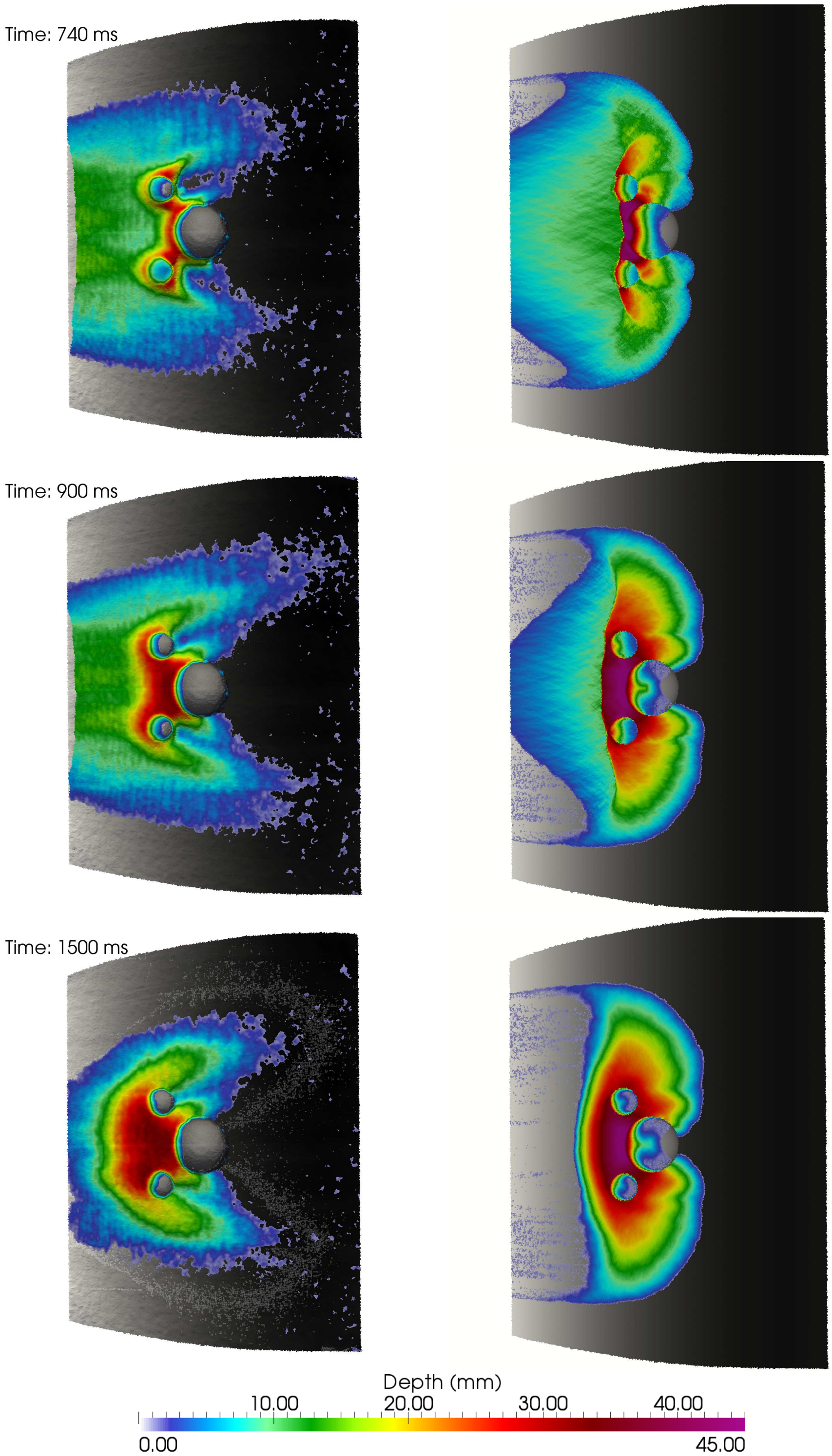

Figure 21: Section 5.2. 2D plant views for the sand depth obtained experimentally (left side) and computationally (right side) at times t = 740 ms, t = 900 ms, t = 1500 ms

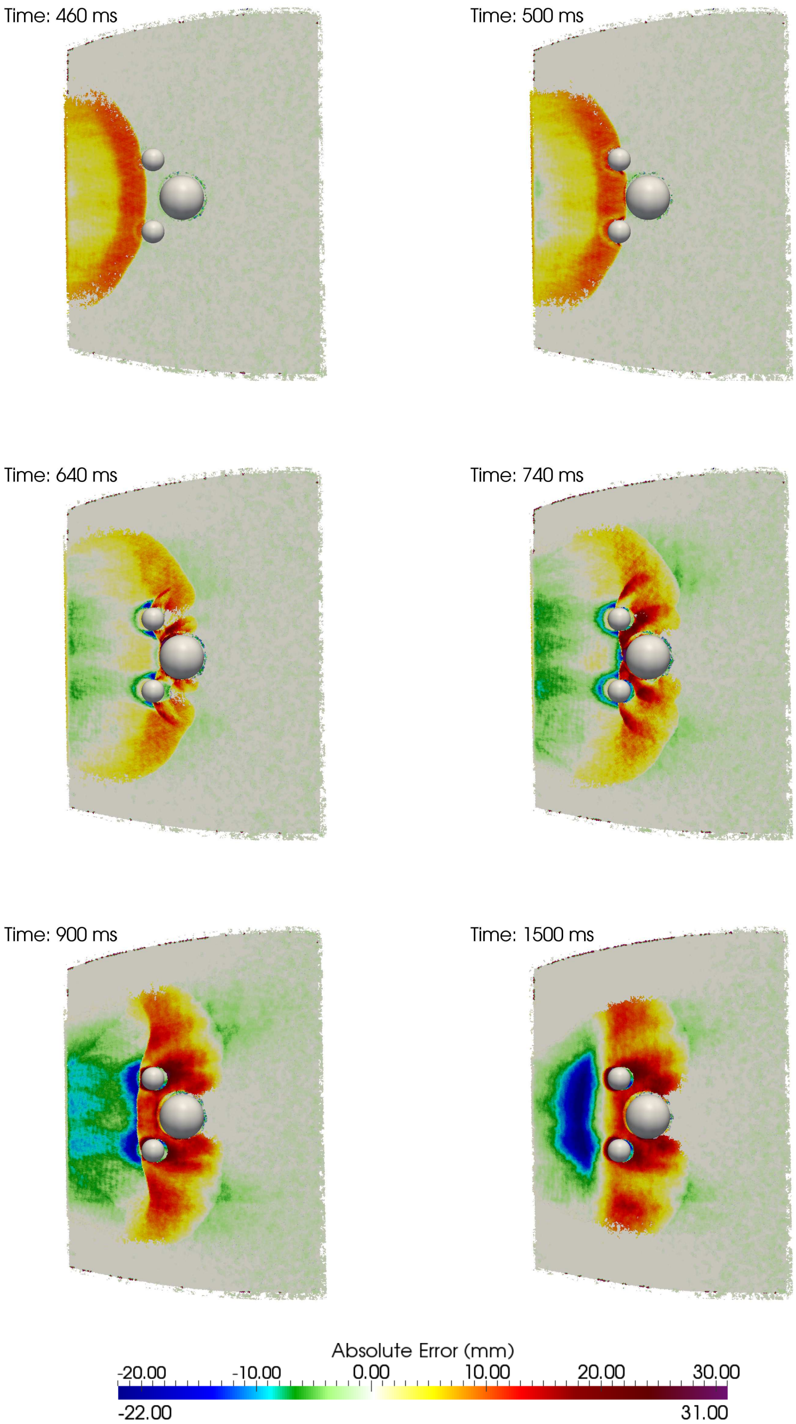

Figure 22: Section 5.2. 2D plant views displaying the absolute error at times $t = 460$ ms, $t = 540$ ms, $t = 640$ ms, $t = 740$ ms, $t = 900$ ms, $t = 1500$ ms

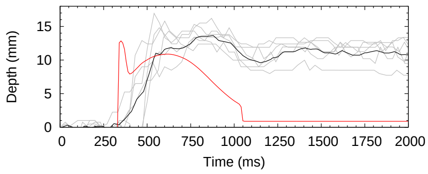

(a) PD1

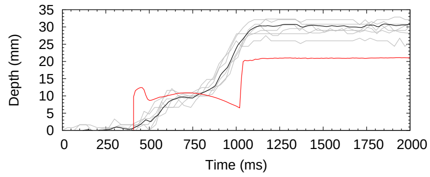

(b) PD2

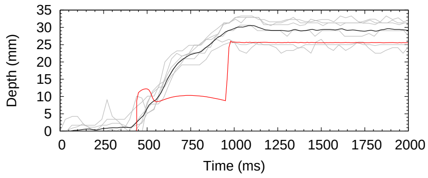

(c) PS1

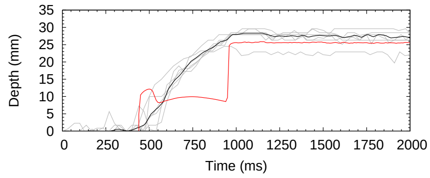

(d) PS2

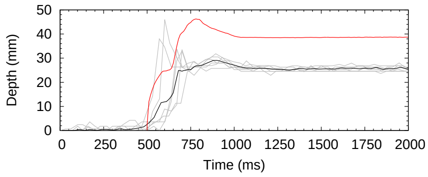

(e) PSL

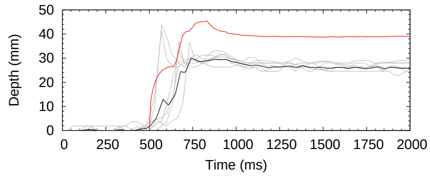

(f) PSR

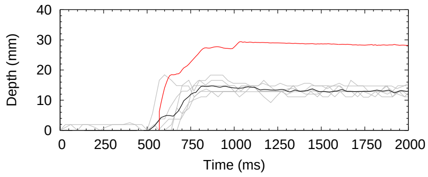

(g) PS0L

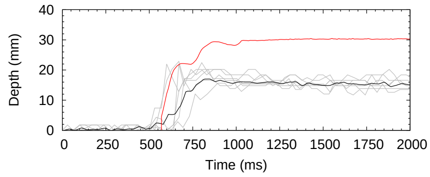

(h) PS0R

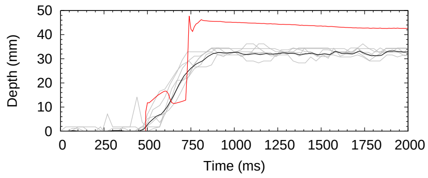

(i) PS0

Figure 23: Section 5.2. Computational and experimental probe results

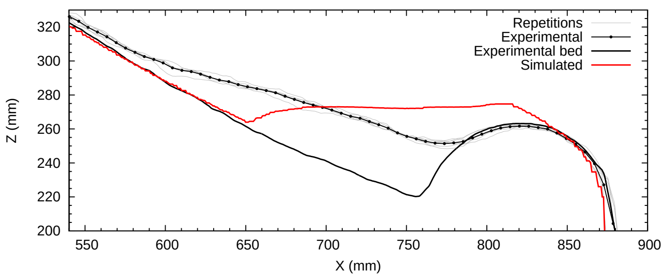

Figure 24: Section 5.2. Longitudinal section ($y = 500\,mm$) for Experiment 2 at the final stage

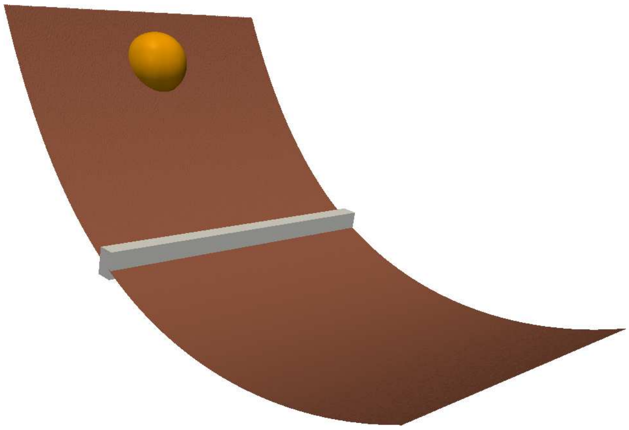

Figure 25: Section 5.3. Initial configuration with the sand deposit at the beginning of the slope and the dike downwards

5.3. Gravity driven flow facing up a dike

Another important configuration in real applications is an oncoming flow against barriers. The design and location of this type of structures highly governs the dynamical description of the granular flow and its final shape. The two principal phenomena observed in this configuration are the presence of deflection waves upstream of the dike and the overtopping generated when the flow depth exceeds the height of the dike crest. Previous works focused on small-scale laboratory experiments with dike structures and granular flows such as the ones by Hakonardottir et al. (2003); Faug et al. (2008). In both works, the granular material was confined in a 1D configuration and the start/go mechanism was not studied in detail, as no data about the plan view spreading of the material was provided. The spreading of the landslide against a dike is an active topic as it was stated in Johannesson et al. (2009).

Figure 25 shows a 3D view of the initial configuration of the experiment.

Figure 26 displays a temporal sequence of 3D views. Once the sand is released on the top of the slope the flow is accelerated downwards. The inertia of the moving mass is high enough for it to fly over the dike, for example at times $t = 490\,ms$, $t = 610\,ms$. Nevertheless, the most of the mass is retained by the dike structure, and the maximum run out of the avalanche is highly shortened by the dike effect, see times $t = 710\,ms$ and $t = 910\,ms$. At time $t = 1040\,ms$ most of the morphodynamic changes have taken place and at time $t = 2000\,ms$ the mass has reached an equilibrium stage.

Comparison with the experimental data is shown in Figures 27 and 28.

At times $t = 490\,ms$ and $t = 610\,ms$ the computational results are affected by the time lag of the sand release procedure. Afterwards, differences among the instants of time are located in the tail of the avalanche. In the computational results the tail moves faster than in the experimental data and consequently, the depth elevation upstream from the dike is higher and in the tail region it is smaller. These differences during the transient stage of the avalanche are reduced once the equilibrium stage is reached, at time $t = 2000\,ms$. The front and the tail of the avalanche are well reproduced by the numerical model. The maximum run out obtained with the computational model tends to be slightly underestimated. This can be justified by the high level of energy that the grains have during the avalanche and that allow them to fly further downstream from the dike. With the depth averaged assumption considered in this work, the vertical acceleration is neglected and consequently, the vertical motion is underestimated.

Additionally, at this temporal stage, the constant slope of granular material upstream from the dike clearly identified in the companion work is also easily distinguishable.

The transient absolute errors are displayed in Figure 29. As it has been explained above, the larger differences at times $t = 490\,ms$, $t = 610\,ms$ and $t = 710\,ms$ are found at the front and at the tail, since in the computed results, the head of the avalanche moves faster and the sand accumulates upstream from the dike and at the tail. Nevertheless, the final stage provides a limited error all over the domain. At that time, the main error area is located in the middle of the slope material accumulated upstream from the dike. This is consistent with the phenomena observed at the plan views, Figure 28 at time $t = 2000\,ms$, since in the numerical solution the area with constant slope is wider than in the experimental data. Moreover, the quasi zero error area located on the top of the dike, i.e. the overtopping area, at the final stage is remarkable. Computational and experimental data match accurately.

The computational results are also validated against the probe results obtained in the companion work, but excluding PS0R, PS0L and PS0 because they showed no information in this experimental case, Figure 30. As it has been noted in the previous experiments, the probes located upslope are more influenced by the sand release procedure. Consequently, a temporal lag in the peak flow is observed at probes PU and PD1. Probe PD2 display an accurate tracking of the temporal evolution of the sand depth evolution. PS1 and PS2 present a good trend of the experimental dynamics although the surface level is underestimated downwards the dike. This is coherent with the 2D views shown in Figure 28 at time $t = 2000\,ms$: the maximum run out is slightly shorten in the computational solution.

Figure 31 shows the longitudinal section at $y = 500\,mm$. Regarding the observed computed and experimental bed topography differences, i must be noted that the conceptual model is depth averaged and the region downstream from the dike can not be correctly described. Therefore, it has been decided to design a *vertical* dike for the simulation. Nevertheless, both computational and experimental data display the same tendency, describing a uniform slope upstream from the dike. The main differences are focused on the tail, where numerical solution presents a more severe slope. Additionally, the maximum run out is overestimated with the computed prediction, which is justified by the highly fluidized mass observed in the laboratory work, which allows the material granular to fly further during the overtopping event.

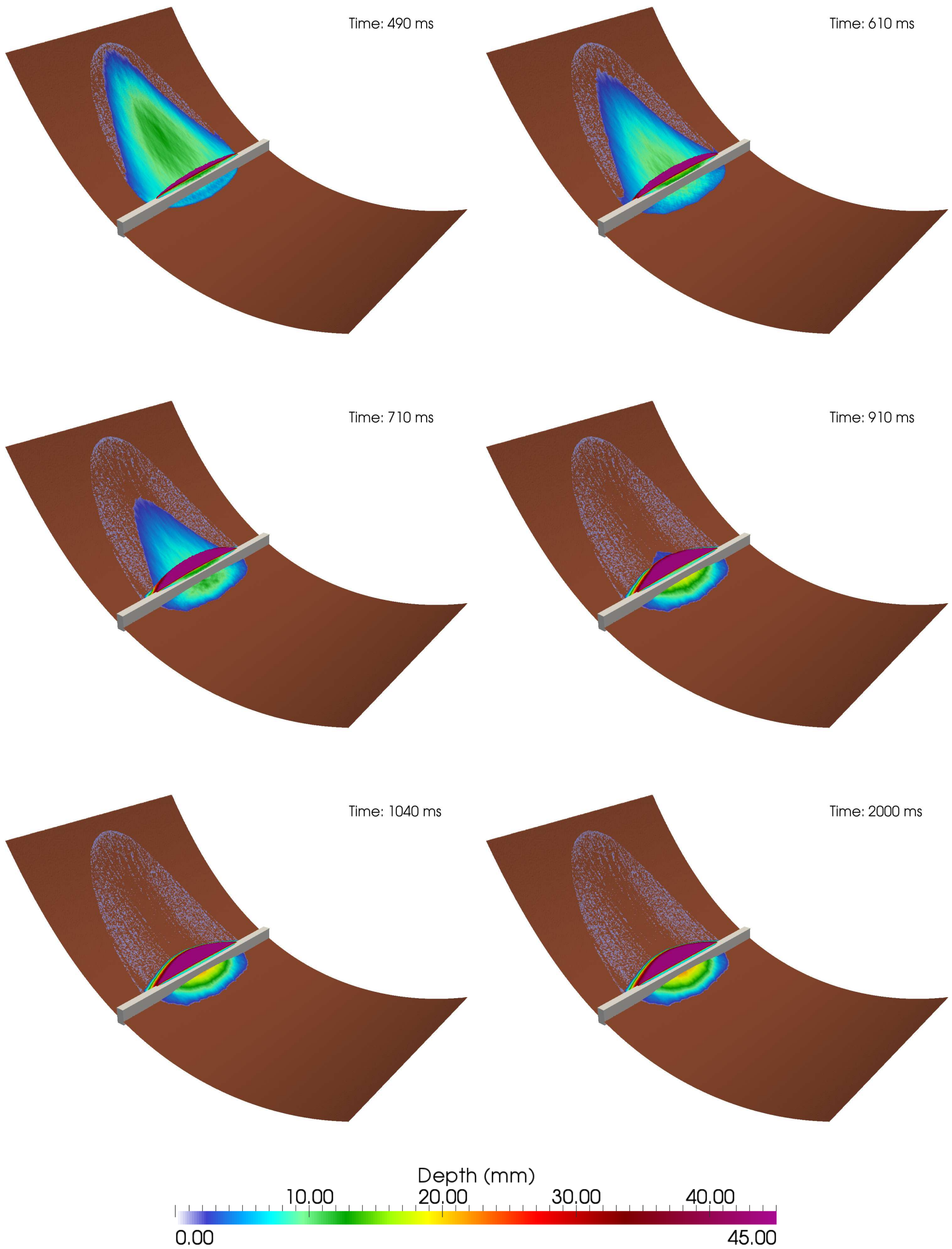

Figure 26: Section 5.3. 3D contour views for the free surface level at times t = 490 ms, t = 610 ms, t = 710 ms, t = 910 ms, t = 1140 ms and t = 2000 ms

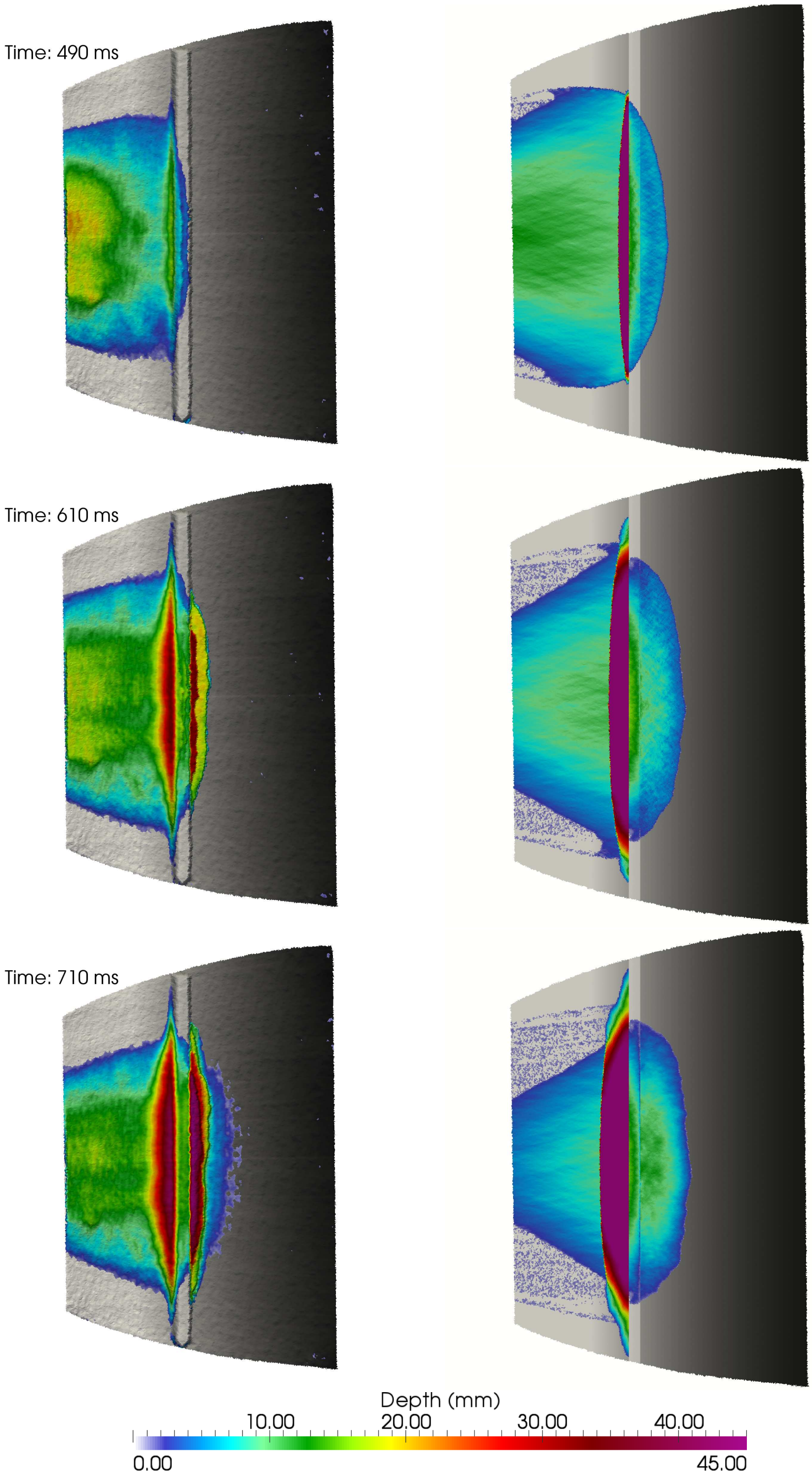

Figure 27: Section 5.3. 2D plant views for the sand depth obtained experimentally (left side) and computationally (right side) at times $t = 490$ ms, $t = 610$ ms, $t = 710$ ms

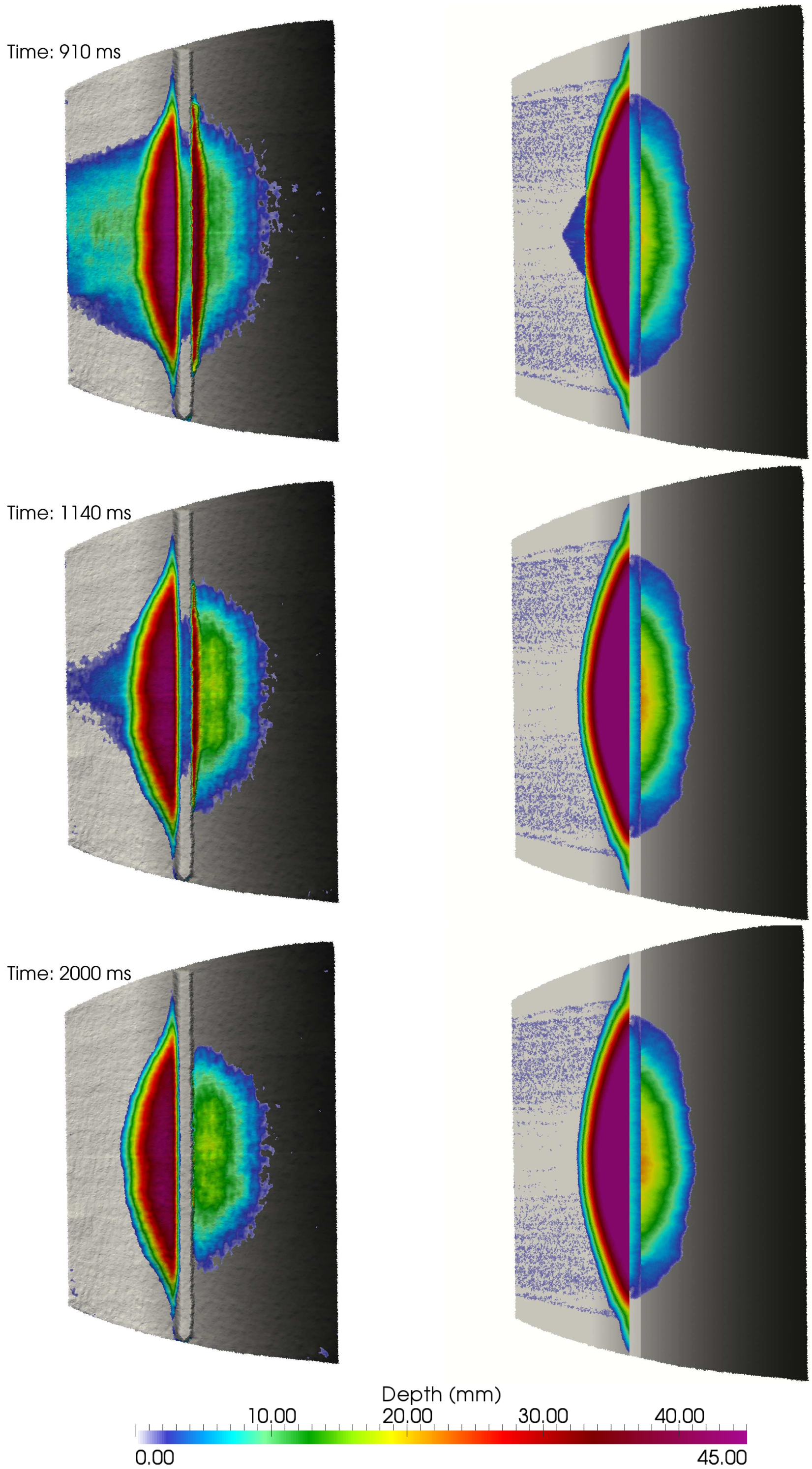

Figure 28: Section 5.3. 2D plant views for the sand depth obtained experimentally (left side) and computationally (right side) at times $t = 910$ ms, $t = 1140$ ms, $t = 2000$ ms

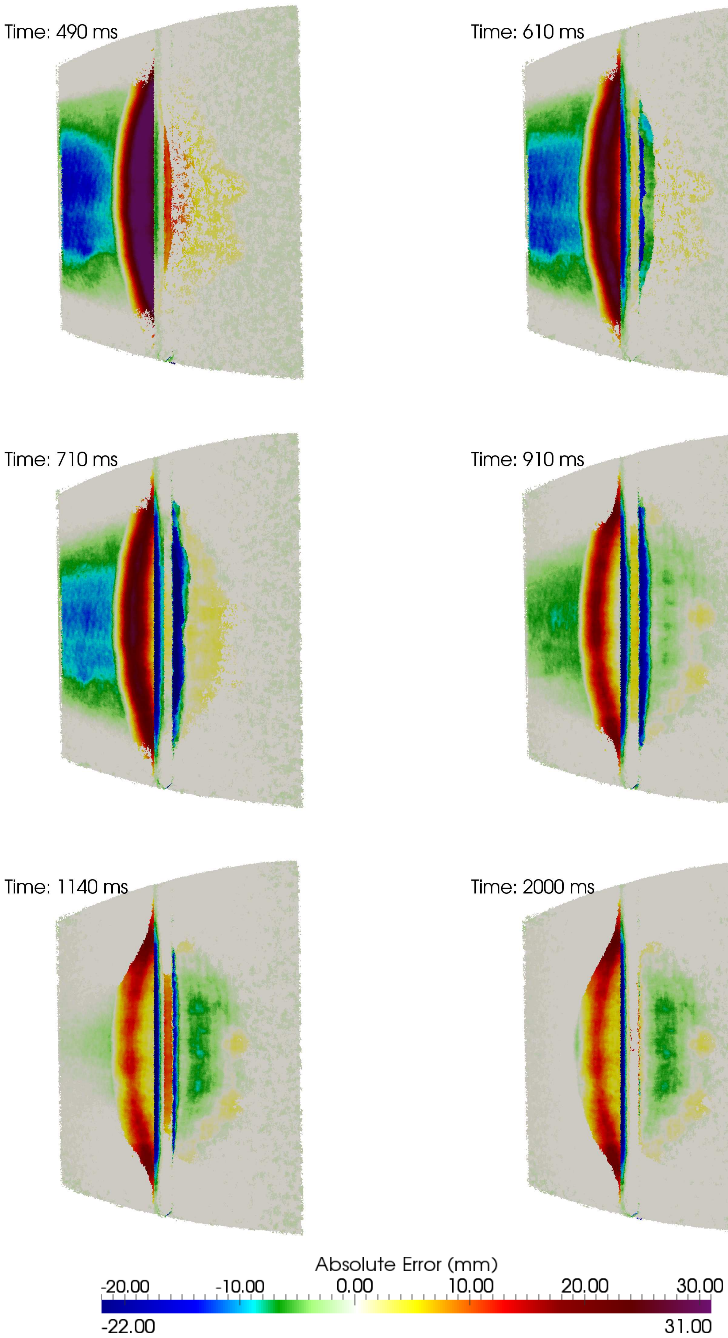

Figure 29: Section 5.3. 2D plant views displaying the absolute error at times $t = 490$ ms, $t = 610$ ms, $t = 710$ ms, $t = 910$ ms, $t = 1140$ ms, $t = 2000$ ms

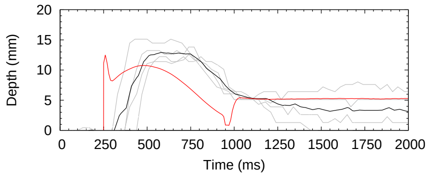

(a) PU

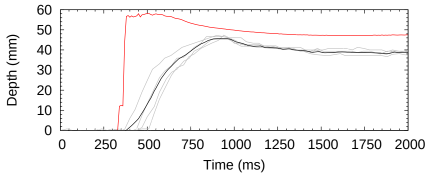

(b) PD1

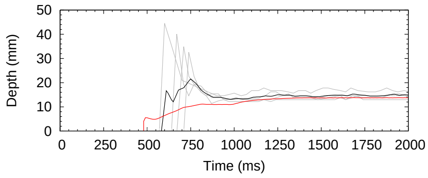

(c) PD2

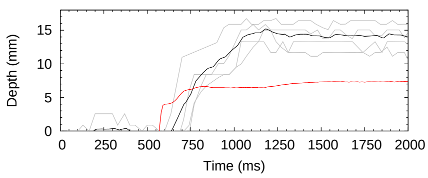

(d) PS1

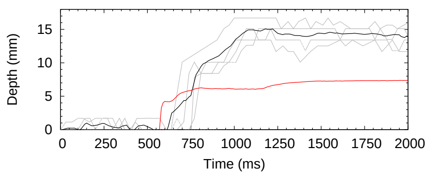

(e) PS2

Figure 30: Section 5.3. Computational and experimental probe results

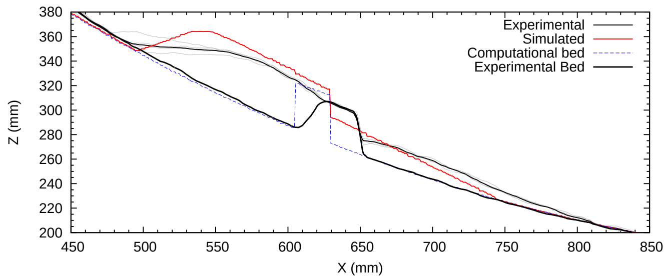

Figure 31: Section 5.3. Longitudinal section ($y = 500\,mm$) for Experiment 3 at the final stage

6. Conclusions

In the present work dry granular flow has been simulated using a 2D Finite Volume scheme previously validated in Murillo and García-Navarro (2012) to predict the stop/go mechanisms of the flow behavior but considering the features of gravity projections derived for unstructured meshes in Juez et al. (2013). Fluxes and source term discretization were obtained from the analysis of quiescent equilibrium, prior to being included in the approximate Riemman Problem. These characteristics make the numerical scheme an adequate tool to verify its capacities under a series of experimental cases, which represent small-scale up-to-date environmental problems.

The development of the laboratory work and the measurement technique employed is fully described in the companion work. The main singularity of the experiments is focused on the presence of obstacles, over a rough and complex topography, which in turn implies shock formation. These moving shocks are the key for the understanding of the flow behavior and are well reproduced by the numerical scheme considered. Three experiments have been modeled and analyzed.

The first experiment is based on granular flow around a semispherical obstacle. The computed results are able to accurately track in time the movement and spreading of the mass. Additionally, the two phenomena observed during the development of the experiment, namely the stagnation area upstream from the obstacle and the shock around it, are also numerically reproduced.

The second experiment consists of granular flow around two small semispherical obstacles and one semispherical obstacle located downstream. The complexity of this case is larger, since the shock structure involves the presence of additional moving waves which interact with each other. Nevertheless, the temporal prediction of the computed results displays a good agreement in comparison with experimental data.

The third experiment is of granular flow over a square dike where a overflow takes place. The temporal prediction and the maximum run out are well reproduced by the numerical model.

The main flow structures are well captured in time and space by the numerical scheme in the three experiments: the impact, the shock formation, the overflow and the maximum run out. The small differences in the shocks are justified by the depth averaged assumption considered, as the vertical accelerations around the obstacles are neglected. Moreover, thanks to the robustness of the numerical scheme, able to handle with complex stop/go conditions and wet/dry situations, distorting numerical effects are avoided. Hence, the forecasting capabilities of the computed results can be used for the future design of civil infrastructures or for the understanding of more complex and ambitious rheological models.

7. Acknowledgements

This work was partially supported and funded by the Spanish Ministry of Science and Technology under research project CGL2011-28590. The authors would like to thank Dr. Borja Latorre for his support with setting up the RGB-D sensor as well as Edoardo Cogliandro and Alberto Blein for their support in preparing and calibrating the experimental facility.

Bibliography

Bouchut, F., Fernández-Nieto, E.D., Mangeney, A., Lagrée, P.Y., 2008. On new erosion models of Savage-Hutter type for avalanches. Acta Mechanica 199, 181–208.

Bouchut, F., Mangeney-Castelnau, A., Perthame, B., Vilotte, J., 2003. A new model of Saint-Venant and Savage-Hutter type for gravity driven shallow water flows. C. R. Acad. Sci. Paris Ser. I, 531–536.

Boutreux, T., deGennes, P., 1997. Evolution of a step in a granular material: the Sinai problem. Comptes rendus de l academie des sciences. Serie II Fascicule B-Mechanique Physique Chimie Astronomie 325, 85–89.

Burguete, J., García-Navarro, P., Murillo, J., García-Palacín, I., 2007. Analysis of the friction term in the one-dimensional shallow-water model. Journal of Hydraulic Engineering 133, 1048–1063.

Cui, X., Gray, J., 2013. Gravity-driven granular free-surface flow around a circular cylinder. Journal of Fluid Mechanics 720, 314–337.

Da Cruz, F., Emam, S., Prochnow, M., Roux, J., Chevoir, F., 2005. Rheophysics of dense granular materials: Discrete simulation of plane shear flows. Physical Review 72, 021309.

Douady, S., Andreotti, B., Daerr, A., 1999. On granular surface flow equations. The European Physical Journal B 11, 131–142.

Ertas, D., Grest, G., Halsey, T., 2001. Gravity-driven dense granular flows. Europhysics Letters 56(2), 214–220.

Faug, T., Gauer, K., Lied, K., Naaim, M., 2008. Overrun length of avalanches overtopping catching dams: cross-comparison of small-scale laboratory experiments and observations from full-scale avalanches. Journal of Geophysical Research 113, F03009.

Faug, T., Naaim, M., Naaim-Bouvet, F., 2004. Experimental and numerical study of granular flow and fence interaction. Annals of Glaciology 38, 135–138.

Favreau, P., Mangeney, A., Lucas, A., Crosta, G., Bouchut, F., 2010. Numerical modeling of landquakes. Geophysical Research Letters 37, L1530.

Forterre, Y., Pouliquen, O., 2003. Long-surface-wave instability in dense granular flows. Journal of Fluid Mechanics 486, 21–50.

Gray, J., Tai, Y., Noelle, S., 2003. Shock waves, dead zones and particle-free regions in rapid granular free-surface flows. Journal of Fluid Mechanics 491, 161–81.

Gray, J., Wieland, K., Hutter, K., 1999. Gravity-driven free surface flow of granular avalanches over complex basal topography. Proc. Royal Soc. London Ser. A, 455, 1841.

Hakonardottir, K., Hogg, A., 2005. Oblique shocks in rapid granular flows. Physics of Fluids 17, 077101.

Hakonardottir, K., Hogg, A., Batey, J., Woods, A., 2003. Flying avalanches. Geophysical Research Letters 30, 2191.

Hauksson, S., Pagliardi, M., Barbolini, M., Johannesson, T., 2007. Laboratory measurements of impact forces of supercritical granular flow against mast-like obstacles. Cold Regions, Science and Technology 49, 54–63.

Hungr, O., McDougall, S., 2009. Two numerical models for landslide dynamci analysis. Computers and Geosciences 35, 978–992.

Johannesson, T., Gauer, P., Issler, P., Lied, K., 2009. The design of avalanche protection dams: recent practical and theoretical develpments. Technical Report Europa 23339, European Commision.

Johnson, P., Jackson, R., 1987. Frictional-collisional constitutive relations for granular materials, with application to plane shearing. Journal of Fluid Mechanics 176, 67–93.

Juez, C., Murillo, J., García-Navarro, P., 2013. 2D simulation of granular flow over irregular steep slopes using global and local coordinates. Journal of Computational Physics 255, 166–204.

Kerswell, R., 2005. Dam break with Coulomb friction: A model for granular slumping? Physics of Fluids 17.

Lajeunesse, E., Mangeney-Castelnau, A., Villote, J.P., 2004. Spreading of a granular mass on a horizontal plane. Physics of Fluids 16, 2371–2381.

Louge, M., 2003. Model for dense granular flows down bumpy inclines. Physical Review 67, 061303.

Mangeney, A., Roche, O., Hungr, O., Mangold, N., Faccanoni, G., Lucas, A., 2010. Erosion and mobility in granular collapse over sloping beds. Journal of Geophysical Research 115, F03040.

Mangeney-Castelnau, A., Bouchut, F., Vilotte, J.P., Lajeunesse, E., Aubertin, A., Pirulli, M., 2005. On the use of Saint-Venant equations for simulating the spreading of a granular mass . Journal of Geophysical Research 110, B09103.

Manning, R., 1895. On the flow of water in open channels and pipes. Transactions of the Institution of Civil Engineers of Ireland 20, 161–207.

Moretti, L., Mangeney, A., Capdeville, Y., Stutzmann, E., Huggel, C., Schneider, D., Bouchut, F., 2012. Numerical modeling of the Mount Steller landslide flow history and of the generated long period seismic waves. Geophysical Research Letters 39, L16402.

Murillo, J., García-Navarro, P., 2012. Wave Riemann description of friction terms in unsteady shallow flows: Application to water and mud/debris floods. Journal of Computational Physics 231, 1963–2001.

Pirulli, M., Bristeau, M., Mangeney-Castelnau, A., Scavia, C., 2007. The effect of the earth pressure coefficients on the runout of granular material. Environmental Modelling and Software 22, 1437–1454.

Pirulli, M., Mangeney, A., 2008. Results of Back-Analysis of the Propagation of Rock Avalanches as a Function of the Assumed Rheology. Rock Mechanics and Rock Engineering 41, 59–84.

Pouliquen, O., 1999. Scaling laws in granular flows down rough inclined planes. Physics of Fluids 11, 542–548.

Pouliquen, O., Forterre, Y., 2002. Friction law for dense granular flows: application to the motion of a mass down a rough inclined plane. Journal of Fluid Mechanics 453, 133–151.

Pouliquen, O., Forterre, Y., 2008. Flows of Dense Granular Media. Annual Review of Fluid Mechanics 40, 1–24.

Roche, O., Attali, M., Mangeney, A., Lucas, A., 2011. On the run-out distance of geophysical gravitational flows: Insight from fluidized granular collapse experiments. Earth and Planetary Science Letters 311, 375–385.

Roe, P.L., 1983. Approximate Riemann solvers, parameter vectors, and difference schemes. Journal of Computational Physics 50, 235–269.

Savage, S., Hutter, K., 1989. The motion of a finite mass of granular material down a rough incline. Journal of Fluid Mechanics 199, 177–215.

Tai, Y., Hutter, K., Gray, N., 2001. Dense granular avalanches: Mathematical description and experimental validation. Lecture Notes in Physics 582, 339–366.

Tai, Y., Kuo, C., 2008. A new model of granular flows over general topography with erosion and deposition. Acta Mechanica 199, 71–96.

Wieland, M., Gray, J., Hutter, K., 1999. Channelized free-surface flow of cohesionless granular avalanches in a chute with shallow lateral curvature. Journal of Fluid Mechanics 392, 73.